**Czech Technical University in Prague**

**Faculty of Nuclear Sciences and Physical Engineering**

**Department of Physics**

# RELATING THE SIGNATURES OF ACTIVELY ACCRETING SUPERMASSIVE BLACK HOLES TO THE COLD GAS CONTENT IN THEIR HOST GALAXIES

## MASTER THESIS

**Bc. Anežka Kabátová**

Field of study:   Experimental Nuclear and Particle Physics

Supervisors:   Ing. Michal Marčišovský, Ph.D.
Dr. Paola Andreani

# Assignment

Zde vlož zadání

# Statement of Authorship

I declare that this master thesis has been composed solely by myself and that I have cited all sources I have used in the bibliography.

I have no serious reason against the use of this work in the sense of § 60 of Act No. 121/2000 Sb., On Copyright, on Rights Related to Copyright and on Amendments to Certain Acts (Copyright Act).

Prohlašuji, že jsem svou diplomovou práci vypracovala samostatně a použila jsem pouze podklady uvedené v přiloženém seznamu.

Nemám žádný závažný důvod proti použití tohoto školního díla ve smyslu § 60 Zákona č. 121/2000 Sb., o právu autorském, o právech souvisejících s právem autorským a o změně některých zákonů (autorský zákon).

V Praze 11. srpna 2020

_____

Podpis

iv

# Acknowledgement

*Title of Master Thesis:*

**Relating the Signatures of Actively Accreting Supermassive Black Holes to the Cold Gas Content in Their Host Galaxies**

*Author:*      Bc. Anežka Kabátová

*Field of study:*      Experimental Nuclear and Particle Physics

*Type of Work:*      Master Thesis

*Supervisors:*      Ing. Michal Marčišovský, Ph.D.,
*Department of Physics,*
*Faculty of Nuclear Sciences and Physical Engineering,*
*CTU in Prague*

Dr. Paola Andreani,
*European Southern Observatory*

*Consultants:*      Ing. Mária Marčišovská, Ph.D.,
*Department of Physics,*
*Faculty of Nuclear Sciences and Physical Engineering,*
*CTU in Prague*

Dr. Dominika Wylezalek,
*European Southern Observatory*

*Abstract:* This work focuses on the influence of the active galactic nuclei on the environment of their host galaxy. The galaxy evolution, driven by both inner and outer processes, remains one of the most prominent open questions of astrophysics. The accreting supermassive black hole in the center of galaxies plays a key role in their further development through positive and negative feedback mechanisms. Within this work, the cold gas content of galaxies possessing an active galactic nucleus is studied and linked to the size of the narrow line region around it. The size of the narrow line region serves as a proxy of the central black hole activity which is assumed to cause the depletion of cold gas that leads to the shutdown of star formation within the host galaxy. With the growth of the integral field spectroscopy, it is possible to study spatially resolved galactic properties. This work engages MaNGA data combined with radio-data from Arizona Radio Observatory under the MASCOT project.

*Autor:*  Bc. Anežka Kabátová

*Obor studia:*  Experimentální jaderná a částicová fyzika

*Druh práce:*  Diplomová práce

*Školitelé:*  Ing. Michal Marčišovský, Ph.D.,
*Katedra fyziky,*
*Fakulta jaderná a fyzikálně inženýrská,*
*ČVUT v Praze*

Dr. Paola Andreani,
*Evropská jižní observatoř*

*Konzultanti:*  Ing. Mária Marčišovská, Ph.D.,
*Katedra fyziky,*
*Fakulta jaderná a fyzikálně inženýrská,*
*ČVUT v Praze*

Dr. Dominika Wylezalek,
*Evropská jižní observatoř*

*Abstrakt:* Tato práce je zaměřena na studium vlivu aktivních galaktických jader na prostředí jejich hostitelských galaxií. Evoluce galaxií, podléhající vnitřím i vnějším procesům, zůstává jednou z nejdůležitějších otevřených otázek astrofyziky. Akreující supermasivní černá díra v centru galaxií pravděpodobně hraje klíčovou roli v jejich dalším vývoji prostřednictvím pozitivní i negativní zpětné vazby. V této práci je studován obsah chladného plynu v galaxiích disponujících aktivním galaktickým jádrem a je spojen s velikostí regionu úzkých emisních čar v jeho okolí. Oblast úzkých emisních čar slouží jako ukazatel aktivity centrální černé díry. Předpokládá se, že právě ona způsobuje úbytek chladného plynu, který vede k zastavení tvorby hvězd v její hostitelské galaxii. S rozvojem spektroskopie celého pole (integral field spectroscopy) je možné studovat prostorově rozlišené vlastnosti galaxií. Tato práce využívá dat z experimentu MaNGA v kombinaci s daty v rádiové oblasti z Arizonské radiové observatoře v rámci projektu MASCOT.

*Klíčová slova:*  Aktivní galaktická jádra, Oblast úzkých emisních čar, Obsah chladného plynu, Spektroskopie celého pole

# Contents

# Acronyms

**AGN** Active galactic nucleus

**ALMA** Atacama Large Millimeter Array

**ARO** Arizona Radio Observatory

**BPT Diagram** Baldwin, Phillips, Telervich Diagram

**CCD** Charge-coupled Device

**DAP** Data Analysis Pipeline

**DRP** Data Reduction Pipeline

**FITS** Flexible Image Transport System

**HI** Neutral hydrogen

**HII** Ionized hydrogen

**IFS** Integral field spectroscopy

**IFU** Integral field unit

**IR** Infrared

**ISM** Interstellar medium

$\mathbf{L}_\odot$ Luminosity of the Sun

$\mathbf{M}_\odot$ Mass of the Sun

**MLA** Microlens array

**MOS** Multi-object Spectroscopy

**NGC** New General Catalogue

**NLR** Narrow-line region

**PSF** Point spread function

**RSS** Row-stacked Spectra

**UV** Ultraviolet

# 1 Introduction

The feedback of active galactic nuclei (AGN) on their host galaxies is one of the central questions of the present astrophysics. There is no consensus on the exact role of the AGN in the development of its host galaxy [1]. One of the scenarios is that the spatial extension of the AGN-ionised region anticorrelates with the content of molecular gas that is crucial for further development of the galaxy itself. The MASCOT survey is aiming to answer this question by combining data from the MaNGA survey and the Arizona Radio Observatory (ARO). The size of the narrow-line region (NLR) of the galaxies derived from the MaNGA data can be compared to the CO luminosity that is a measure of the molecular gas content provided by ARO. Because the MASCOT survey is currently ongoing, only a limited number of targets is available for the comparison. However, this thesis serves as a basis for further investigation, along with the algorithms created within the scope of this thesis.

The correlations of the properties of supermassive black holes and their host galaxies have been widely observed. The suggested scenario states that the black hole co-evolves with the bulge of the host galaxy with little if any correlation with the subsequent disk formation, as shown among many others by Ferrarese et al. [2], Gebhardt et al. [3] and recently by Gaspari et al. [4], who revealed some new scaling relations. The co-evolution goes in both directions - the black hole needs the interstellar medium (ISM) of specific properties for its growth and the ISM is subsequently influenced by the activity of the black hole. At least some of the observed relations can be explained by merging and interactions of galaxies that, as explained in Section 3, can ignite both the star formation and the AGN activity by supplying the galaxy with gas. However, the AGN-galaxy co-evolution is a complex topic that is at the center of focus of the current research.

The AGN influence on star formation is the key component of the overall understanding of the process. Apparently, the feedback can be both positive and negative. Examples of the positive feedback can be found in works of Silk [5] and Cresci and Maiolino [6] who show that the outflow and winds from the AGN can cause the pressure-induced star formation in the gas-rich disks. The negative feedback is caused by the mechanical ejection of the ISM from the central regions of the galaxy as shown e.g. in the work of McNamara et al. [7] and by the heating of the gas that can lead to the quenching of star formation. The significance of these processes is still an open question. Some studies suggest that outflows from the AGN are depleting the region along their path, quenching star formation

locally, but also trigger star formation at different parts of the galaxy [8].
The rapidly growing field of integral field spectroscopy (IFS) introduced
in Section 4 can shed a light on this topic by revealing the correlations between
the position of the AGN outflows and the star formation, among others.
The stated goals for the thesis are as follows:

- Create an algorithm for the effective and reliable measurement of the size
  of the narrow line region of observed galaxies. This is done by fitting
  the [OIII] surface brightness spatial distribution (from MaNGA)
  by the Sersic profile as explained in following chapters.

- Suggest a method for the measurement of the NLR size of targets that are
  very irregular (e.g. mergers). Since the sample of galaxies observed by both
  MaNGA and ARO and its AGN sub-sample is not very extensive, it is
  desirable to be able to measure the galaxy properties for all the targets, not
  only the regular ones which are easily analysed by the basic algorithm.

- Compare the derived sizes of the narrow line region to the integrated
  properties of the molecular gas, such as CO luminosity, provided by ARO.

All of these tasks shall be done as universally as possible. On the time scale of this
thesis, it is impossible to get statistically significant results. However,
the promising MASCOT project is still ongoing and many more targets will be
observed. For this reason, the thesis is considered to be a starting point
for subsequent work in the upcoming years.

# 2 Galaxies

The first evidence of the presence of different galaxies besides the Milky Way in our Universe was provided by Edwin Hubble in 1920s [9]. Firstly detected by William Parsons in 1845, they were referred to as nebulae due to the insufficient resolution of available telescopes. The equipment Parsons used was among the most advanced in the world at the time, therefore, some of the features of the galaxies were visible already, e.g. the spiral shape. A great debate, ignited over whether the "clouds of stars" were within or outside of our own galaxy, is referred to as Shapley-Curtis debate after astronomers Harlow Shapley and Heber D. Curtis. Finally, in 1924, Curtis was proven right by the Hubble's observation. Using a telescope on Mount Wilson in California, Hubble discovered variable stars in the Andromeda galaxy. Following a law used for the estimate of the distance of Cepheids[1],

$$F = \frac{L}{4\pi d^2},\qquad(2.1)$$

where $F$ is the measured flux, $L$ is the luminosity and finally, $d$ is the distance of the star, he proved that the observed stars are at least 300 kpc[2] away from the Galaxy. The Andromeda galaxy, lying in reality 800 kpc from the Milky Way, became the first discovered galaxy [11].

Hubble continued his work in the field and introduced three categories of galaxies within a classification system in Figure 2.1 that is still - with later modifications - nowadays used. Today, the three types are elliptical, spiral and lenticular galaxies. Galaxies that would not fit in any of these categories are called irregular [9].

An overview of the morphology, composition and properties of galaxies follows.

## 2.1 Morphology

*Elliptical galaxies* are objects lacking significant features like spiral arms. They can be further divided according to their shape to sphericals - E0 - or highly elongated ellipticals - E7 (and everything in between). Their stars are generally old because ellipticals do not have additional cold gas material for new star formation. For this

---

[1]Cepheids, or Cepheid variables, are unstable stars changing periodically in radius and temperature which causes regular variation in their luminosities. The well-studied relation between the dimming period and the brightness can be used to determine their distance [10].

[2]Parsec (pc) is the distance at which 1 astronomical unit (AU) subtends an angle of 1 arcsecond. It is equal to approximately 3.26 light years [10].
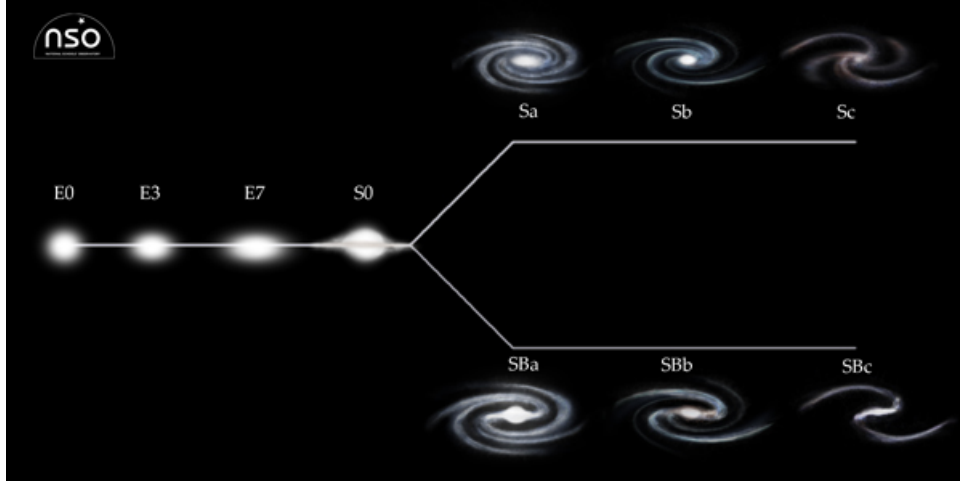
Fig. 2.1. The Hubble's "tuning fork". The scheme shows the basic classification of galaxies. Hubble's assumption was that the galaxy evolution goes from the left (the early-type galaxies) to the right (the late-type galaxies). The elliptical galaxies are sorted from the most spherical shape (E0) to the most elliptical (E7). At the center, there is a lenticular galaxy with common properties of both types (S0). In the upper right part of the scheme, spirals with the spherical nucleus are shown from the most tightly bound (Sa) to ones that have bigger interstellar matter proportion in the disk and whose arms are therefore more open (Sc). The bottom part shows barred galaxies following the same order [12].

reason, they appear reddish in comparison to young-star-dominated spirals. The inner motion is vastly random, without organized or preferred direction. This is true particularly for the most luminous ellipticals with luminosities several times that of the Milky Way. The less luminous ellipticals show some rotation of the stars and formation of the disk within the elliptical body. Hubble wrongly assumed that spiral galaxies gradually evolve from ellipticals. For this reason, ellipticals are sometimes called early-type galaxies. Nowadays, the inverse direction of the evolution is accepted. The elliptical galaxies probably originate from a merger of spirals or other galaxy evolution processes. Nevertheless, the distinction of early- and late-type galaxies still remains active in the community [9].

*Spiral galaxies*, named after dense regions forming bright spiral arms, are rich in newly formed stars. Recent star formation, especially in the spiral arms, is the reason of their brightness. In the center of spirals, there is a bulge with properties similar to elliptical galaxies. This bulge can be symmetrical or barred, which is a base of the further division of spirals. Both barred and unbarred spiral galaxies have additional sub-types according to the relative importance of the central bulge with respect to the disk starting with Sa (SBa, where the additional "B"stands for the spiral *barred* galaxy, respectively) whose spiral arms are closely bound to the bulge. While the fraction of the gas and young stars in the disk increases, the arms are more open [11]. Milky Way is close to Sc, the Andromeda galaxy is Sb. The sequence ends with Sd and SBd gallaxies, where arms are not clearly ordered any more. The extreme case are *magellanic* galaxies, such as the Large Magellanic Cloud, where the spiral is usually reduced to one arm only. The rotation of such

objects is slower. The velocity of 80 km s$^{-1}$ is only about one third of the velocity of Milky Way rotation at the location of the Sun [9].

*Lenticular galaxies* have a central elliptical bulge and rotating disk similar to spirals but without any arms. Like ellipticals, they are neither gas- nor dust-rich. Being similar to both types, they are in the middle of the Hubble's diagram. Lenticulars and ellipticals share one more property - they constitute the majority of the galaxy clusters and groups population [9].

In the local universe, roughly 70% of bright galaxies are spirals, 30% are ellipticals and lenticulars and the small fraction of galaxies of different properties are irregulars [9]. However, this proportion is biased by the fact that spirals with their young and bright stars are more easily detectable. Some estimates say that ellipticals are actually more common than spirals [11].

*Irregular galaxies* are typically smaller and less luminous than spiral galaxies but they undergo an intense star formation process. Their population is a mixture of young and old stars [11].

When Edward Hubble was sorting the galaxies he observed, he was relying on the visible wavelengths. At the present time we know that such bias has a huge influence on the result - most of the visible light of the galaxy is produced by hot stars. However, the cooler stars emitting in infrared region are more numerous and can build structures that are invisible by looking at the more energetic band only [11]. There are several catalogues of galaxies. The oldest one dates back to 18th century, when Charles Messier listed over a hundred of objects of same properties not knowing that they are distant galaxies. The New General Catalogue (NGC) contains more than 7000 objects. Apart from galaxies, NGC lists globular clusters or nebulae and was created in phases from 1888 to 1908. The most pronounced modern catalogues are the Third Reference Catalogue of Bright Galaxies and Uppsala General Catalogue of Galaxies [9].

## ◼ 2.2 Composition

Since ellipticals and lenticulars do not have such a prominent structure compared to spirals, the composition of galaxies such as Milky Way will be described. A typical spiral galaxy consists of a thin and thick disk, a central bulge and a halo as shown in Figure 2.2. 95% of stars are located in the thin disk along with the majority of gas and dust. In the case of the Milky Way, whose stellar disk stretches out to at least 15 kpc, the height of the thin disk is only 300 - 400 pc [9]. Most of the light of the disk is produced by extremely luminous O and B type stars[3] which are, however, very rare. The most abundant stars are similar to the Sun: middle-mass and low-mass main sequence stars followed by red giants [11]. The rest of the stars of the galaxy are in the thick disk with the thickness of 1 kpc. The two populations differ in age and also metallicity. The stars of the thick disk formed earlier in the galaxy evolution when heavy elements were not so abundant. For this

---

[3]Within the Harvard spectral classification, it is possible to divide stars into 7 categories according to their effective surface temperature starting with O stars with the temperature above 30 000 K and ending with M stars with the temperature of 2400 to 3700 K.

reason, the stars of thick disk are metal-poorer. Both the central bulge, whose structure is close to the elliptical galaxy, and the disk are rotating. Stars of the disk follow circular orbits with little random motion. The velocity of the rotation in the case of the disk is approximately 200 km s$^{-1}$. On the other hand, the stars within the central bulge move more randomly, which leads to the lower average speed of about 100 km s$^{-1}$ [9]. A small fraction of the stars can be found in the halo. These stars do not have any organized motion. In the halo, however, most of the globular clusters can be found [11]. Both the bulge and the halo do not contain much gas and dust. The mass comparison of the components reveals the star distribution among them. In the case of the Milky way, the stars of the disk have a mass of $6 \times 10^{10}$ M$_\odot$, the stars of the bulge $2 \times 10^{10}$ M$_\odot$ and the stars of the halo only about $10^9$ M$_\odot$ [9]. The most of the mass of the galaxy lies further than 10 kpc from the galaxy center as can be calculated from the orbital velocities of the galaxy objects. However, 10 kpc is approximately 10 times the size of the thick disk, implying that the mass is not in the form of stars or other visible matter, because this far from the center they are scarce. The dark matter, which is responsible for the most of the mass of the galaxy, forms a roughly spherical dark halo [9].
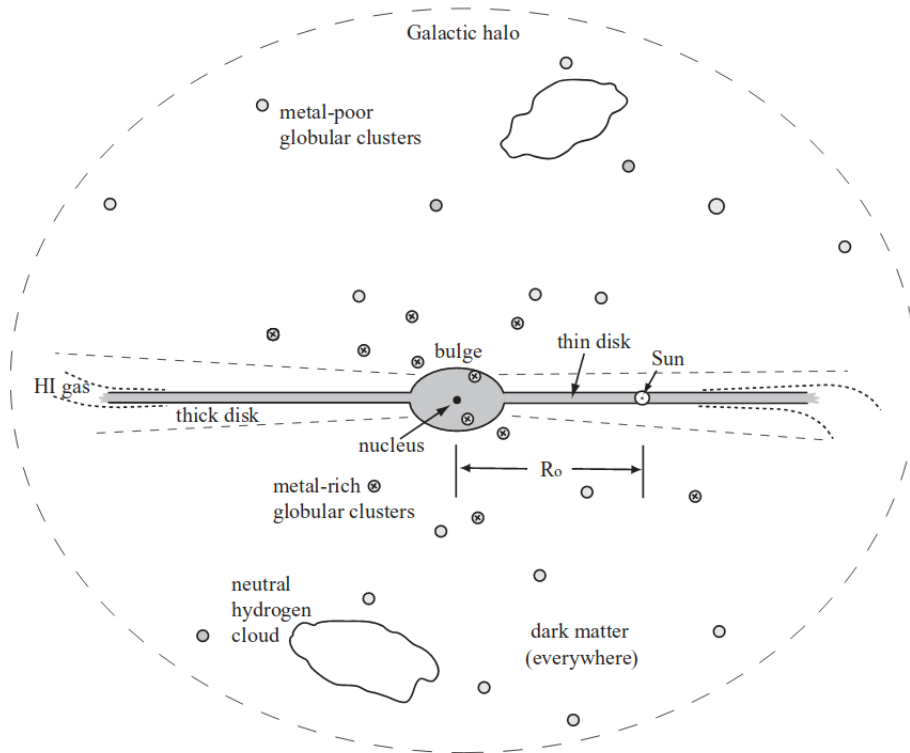


Fig. 2.2. The schematic picture of the Milky Way. The radius of the galaxy is approx. 15 kpc. The Sun is located in the disk plane approx. 8 kpc from the center of the galaxy [9].

# 2.3 Interstellar Medium

The interstellar medium (ISM) consisting of gas, dust and cosmic rays, fills the apparent void within galaxies and is noticeable both from absorption and emission lines in the galaxy spectrum as well as changes of properties of objects observed through it. This broad term includes many different regions of the galaxy − gas in ionized, atomic and molecular phases, etc. For this reason, it is challenging to summarize its properties because some of them will differ in orders of magnitude. In the Milky Way, vast majority of ISM mass is made of hydrogen (70%), followed by helium (28%) and heavier elements (2%). The average density of ISM is as low as 1 particle per cm$^3$. The dust, dramatically changing the ISM properties, constitutes only about 1% of the ISM mass. The dust is composed of carbon, silicates, ice and other complex molecules. The size of the dust particles is in the order of 100 nm  [11].

Objects observed through the ISM appear different than when observed through a fully transparent environment. Two phenomena that demonstrate this behaviour are the *extinction* and the *reddening.* The extinction means that the objects appear dimmer because of the ISM presence which is caused by optical absorption and scattering processes. In the vicinity of the Sun, the extinction is approximately 1 magnitude per 1000 pc. The reddening is caused by the fact that the size of the dust grains is comparable to the shortest wavelengths of the visible light. The blue light is therefore scattered more easily and the objects appear redder. For near-IR wavelengths, the ISM is almost transparent. On the contrary, the mid-IR region, the emission of vibrationally excited molecules within dust grains makes the ISM opaque [11].

The absorption lines of the ISM are easily distinguishable from the stellar ones in several ways. First of all, some absorption lines of the ISM are not present in the spectra of specific stars at all. For example, in the photosphere of the hottest stars, only highly ionized atoms are present. This means that all absorption lines corresponding to atoms that could not survive in the vicinity of such star are clearly coming from the ISM. Even when the spectral lines of the ISM are matching the stellar spectral lines, they can be distinguished by their shape. In stars, material is much denser and hotter than in the ISM, therefore the Doppler broadening of lines caused by the velocity dispersion can be observed. On the other hand, in the ISM the gas is sparse and the lines are sharp. Last but not least, in binary systems, the mutual motion of stars is causing the shifts of the lines in the spectra. The lines that are not moving along with the system's motion are coming from the ISM [11].

The emission spectrum covers the whole wavelength range from radio wavelengths to gamma rays. Among the most prominent emission lines of the ISM is the radio wavelength hydrogen line. It is present only if the environment is not too dense so that the collisions are very rare. The excited hydrogen in the laboratory conditions undergoes the collisional de-excitation to the ground state. However, when the collision is not an option, it can loose energy via the spin-flip and emit a photon with an energy that corresponds to the forbidden transition line of 21 cm. Similarly, other atoms can also produce forbidden lines, such as oxygen [OIII] at

| Atom | Transition | Wavelength | $n_{crit}$ (cm$^{-3}$) |
|---|---|---|---|
| CI | $^3P_1 \to {}^3P_0$ | 610 μm | 500 |
| | $^3P_2 \to {}^3P_1$ | 371 μm | 1 000 |
| CII | $^2P_{\frac{3}{2}} \to {}^2P_{\frac{1}{2}}$ | 158 μm | 50 |
| NII | $^1D_2 \to {}^3P_2$ | 6538 Å | 66 000 |
| | $^1D_2 \to {}^3P_1$ | 6548 Å | 66 000 |
| OI | $^1D_2 \to {}^3P_2$ | 6300 Å | $2 \times 10^6$ |
| | $^3P_1 \to {}^3P_2$ | 63.2 μm | $3 \times 10^4$ |
| | $^3P_0 \to {}^3P_1$ | 145.5 μm | 8 000 |
| OII | $^2D_{\frac{5}{2}} \to {}^4S_{\frac{3}{2}}$ | 3729 Å | 3 400 |
| | $^2D_{\frac{3}{2}} \to {}^4S_{\frac{3}{2}}$ | 3726 Å | 15 000 |
| OIII | $^1D_2 \to {}^3P_2$ | 5007 Å | $7 \times 10^5$ |
| | $^1D_2 \to {}^3P_1$ | 4959 Å | $7 \times 10^5$ |
| | $^1S_0 \to {}^1D_2$ | 4363 Å | $2 \times 10^7$ |
| | $^3P_2 \to {}^3P_1$ | 51.8 μm | 4 000 |
| | $^3P_1 \to {}^3P_0$ | 88.4 μm | 2 000 |
| NeII | $^2P_{\frac{1}{2}} \to {}^2P_{\frac{3}{2}}$ | 12.8 μm | $7 \times 10^5$ |
| NeIII | $^3P_1 \to {}^3P_2$ | 15.6 μm | $2 \times 10^5$ |
| | $^3P_0 \to {}^3P_1$ | 36.0 μm | $3 \times 10^4$ |
| NeV | $^1D_2 \to {}^3P_2$ | 3426 Å | $2 \times 10^7$ |
| SII | $^2D_{\frac{5}{2}} \to {}^4S_{\frac{3}{2}}$ | 6716 Å | 2 000 |
| | $^2D_{\frac{3}{2}} \to {}^4S_{\frac{3}{2}}$ | 6731 Å | 2 000 |
| SIII | $^3P_2 \to {}^3P_1$ | 18.7 μm | $10^4$ |
| | $^3P_1 \to {}^3P_0$ | 33.5 μm | 2 000 |
| SiII | $^2P_{\frac{1}{2}} \to {}^2P_{\frac{3}{2}}$ | 34.8 μm | $3 \times 10^5$ |

Tab. 2.1. Table of common visible and IR spectral lines of forbidden transitions of atoms in non-dense environment [9].

5007 Å. The presence of the forbidden lines can be used for the determination of the maximum density of the gas, before the collisions start to dominate as a way of de-excitation. Such density is called *critical* and is denoted $n_{crit}$ [9]. Table 2.1 shows some common forbidden transitions and wavelengths of the emitted photons widely used in astronomical studies.

More complex molecules are visible through transitions between vibration and rotation energy levels. Examples can be the CO and OH molecules that emit in radio wavelengths. The ionized and excited hydrogen present in HII regions produces the Balmer and Lyman series that correspond to visible and near-UV wavelengths [9]. Infrared lines are produced by atomic hydrogen and water. In the vicinity of high-energy events such as supernovae explosions, emission lines in the UV and X-rays can be produced [11].

The exact shape of the spectrum depends on the local ISM composition and the environment. Cool clouds, within which the gas is neutral, are called HI regions (HI denotes the neutral hydrogen). These regions have density in the order of 100 atoms per cm$^3$ and the dominant emission occurs in radio and IR wavelengths. For

the formation of complex molecules that constitute the molecular clouds, shielding by dust must be provided. When dust absorbs the UV photons coming from stars, such photons can not disrupt the molecules forming in the core of such cloud. The environment is much denser than a common ISM - in the order of 1000 atoms per cm$^3$. The main constituent of the molecular clouds is hydrogen. However, $H_2$ molecules are difficult to detect as they do not have a dipole moment. To trace the molecular gas, CO is usually used with its radio emission at 2.6 mm. These clouds can form extensive regions of the future star formation. The most energetic emission lines come from coronal gas. Although the gas is as hot as $10^6$ K, the density is in the order of hundredths or thousandths of atoms per cm$^3$. It is created by supernova explosions and consists of ionized atoms that produce X-ray photons [11].

Figure 2.3 shows the view of the Milky Way in different wavelength bands. The pictures number 1 and 3 both show the radio continuum at different frequencies (408 MHz and 2.4 - 2.7 GHz). The two continua differ in their source. The first one is coming from synchrotron radiation produced by electrons accelerated in the shock waves from supernovae explosions. The source of the second continuum in the third image is the free-free radiation - bremsstrahlung produced by electrons scattering on ions in the fully-ionized HII regions. The second Milky Way picture is a map of the atomic hydrogen 21 cm radiation. This emission traces HI regions where the atomic hydrogen is present. If the ISM is even colder, so that molecular hydrogen can be formed, the picture number 4 is obtained. The molecular gas clouds are predominantly in the spiral arms marking the sites of the star formation. $H_2$ is not easily detectable so the picture is derived from CO$(1\rightarrow0)$[4] emission which is used as a standard molecular hydrogen tracer. Moving to shorter wavelengths, the fifth picture in combined infrared is mostly formed by the radiation of the dust. Picture number 6 is the mid-infrared picture. The source of this radiation are molecules of polycyclic aromatic hydrocarbons absorbing UV photons and emitting photoelectrons that subsequently effectively heat the atomic gas [9]. The small bright spots in the map are young stars that remain surrounded by the gas cloud from which they were formed. The last of the IR pictures in near-infrared shows mainly K stars emission. In the optical band which is in the eighth picture, the most of the sight is obscured by the dust. The bright red regions are low-density hot gas sites. The blueish glow is caused by scattering of visible light dominantly in short wavelengths. This is also the reason of reddening of the star light. The X-ray image, number 9, comes from the hot gas emission. The last picture shows photons with energies above 300 MeV coming from the collisions of cosmic rays with ions in interstellar clouds. The missing UV band is not presented because it is relatively featureless [13].

# ■ 2.4 Gas Heating and Cooling

From the previous section it is clear that the ISM environment differs dramatically according to its temperature conditions. There are several mechanisms that can

---

[4]CO$(1\rightarrow0)$ denotes the transition between rotational states $J = 1$ and $J = 0$ of the CO molecule.
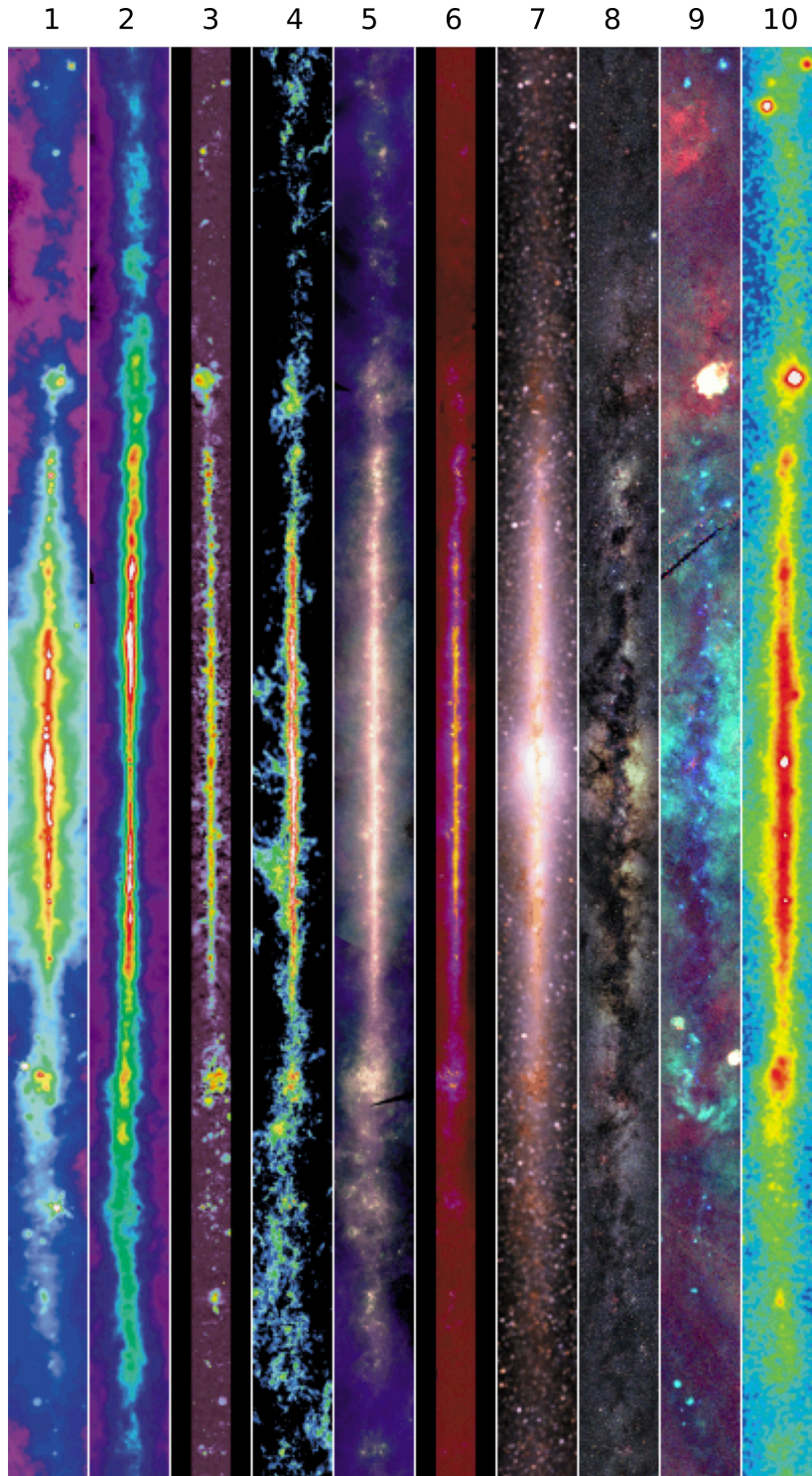
Fig. 2.3. The Milky Way image in different wavelength bands. 1: radio continuum at 408 MHz, 2: atomic hydrogen at 1.4 GHz, 3: radio continuum at 2.4 - 2.7 GHz, 4: molecular hydrogen at 115 GHz, 5: IR picture at $3 - 25 \times 10^3$ GHz, 6: mid-IR, 7: near-IR at $86 - 240 \times 10^3$ GHz, 8: optical image at 460 THz, 9: X-ray image at $6 - 36 \times 10^4$ THz and finally 10: gamma-ray image at frequencies higher than $2.4 \times 10^{10}$ THz, are presented [13].

heat or cool the ISM gas.

The heating can be provided by the low-energy cosmic rays. Since they are abundant and able to penetrate gas clouds, they introduce an effective heating mechanism by excitation, ionization and Coulomb interactions with free electrons. UV photons, possibly emerging from stars, can photo-ionize atoms and molecules. The kinetic energy of the released electron is then used to heat up the medium. In HII regions, there are no photons with energies above 13.6 eV because they have been all used for hydrogen ionization. Therefore, only less-energetic photons can be used for the atomic excitation or ionization. The ionization potential of the carbon is 11.2 eV, so the carbon atoms are responsible for the most of the photoelectric heating in the HII regions. However, this mechanism is not important in the diffuse regions where the abundance of carbon is too low. In these regions, heating by electrons freed from dust grains dominates. In a similar process, dust grain is ionized by an UV photon from a star. The photoelectron then transfers its energy to other free electrons. Because its energy is too low for further ionization, the most of its energy is used to heat up the environment. In addition to UV photons, X-rays can also excite and ionize atoms and the subsequent process of the heating by photoelectron is identical. On the surface of dust grains, chemical reactions take place. Among these, the formation of hydrogen molecule from two hydrogen atoms is the most important process. The energy released by various reactions on the grains is another heating mechanism [14].

The gas cooling is performed by the above-mentioned emissions of the fine-structure photons emitted during the transition from the collisionally-invoked excited state to the lower level. This cooling mechanism dominates the ISM as a whole. However, in molecular clouds, the transitions between vibration and rotation levels of molecules dominates the cooling. Another mechanisms involve the inverse processes of the heating mechanisms - e.g. the recombination on the dust grains that depletes the free electrons from the region [14].

## 2.5 Star Formation

As mentioned above, stars form in the presence of the molecular gas. Because the quenching of the star formation as a consequence of the gas depletion is the subject of this thesis, a summary of the process is provided.

The process starts in a dense cloud of gas which begins to contract under its own gravity. The giant molecular clouds that can eventually form a new star have typically 50 pc in diameter and the mass of $10^5$ M$_\odot$. However, the density of this region is extremely low. Inside the star, it is approximately $10^{20}$ times larger. To make the gas cloud collapse under its gravity, several conditions need to be fulfilled. The thermal motion of the molecules, the magnetic fields affecting the charged particles present in the cloud, the angular momentum conservation of the shrinking gas and turbulences in the interstellar medium all prevent the collapse. Under normal circumstances, the gravity would not dominate and the stars would not form. When the gas cloud is passed by a shock wave, the conditions can, however, change so drastically that the four processes can no longer prevent the

cloud from the collapse. These shocks can occur as a consequence of supernova explosion, stellar winds from newly formed stars or inflow of gas of different density or temperature. The regions where the density is high enough to start the star formation are called *dense cores.* In every giant molecular cloud, there are several dense cores. The cloud collapse is also likely triggered when the gas cloud passes through the spiral arms of the galaxy. These regions are denser, meaning that when the cloud enters, it is compressed. This provides an explanation of the intense star formation in the arms that are, as a consequence, very luminous because of the presence of O and B type stars. The process itself can trigger further star formation via feedback from the newly formed stars and their solar winds as well as supernovae as can be seen in Figure 2.4. Last but not least, two colliding molecular clouds can ignite the star formation [15].

In the stars, the gravity needs to be contra-balanced by the pressure of the radiation from the inside that supports exterior layers. In the stage of a gas cloud, this radiation occurs as the shrinking gas heats up. The velocity, that the free-falling particles gain, leads to their collisions which produce heat. The energy is efficiently radiated away in the form of electromagnetic radiation of such long wavelengths that the gas is effectively transparent. Therefore, the pressure is not high enough to stop the gravitational collapse. The next stage is called a *protostar*. With increasing temperature, the wavelength of the radiation is shorter and shorter, meaning that the gas cloud starts to be opaque. When the radiation cannot escape the cloud any longer, the collapse is not a free-fall any more and further contraction is slow. When the temperature of the core reaches $\sim 10^7$ K, the fusion of hydrogen to helium is ignited. The energy produced by the fusion process is sufficient to prevent the star from further contraction. The gravitational force is balanced by the energy coming from the fusion and star enters the main-sequence phase [15].

Fig. 2.4. Star cluster NGC 602 and surrounding nebulosity around newly formed bright stars. The radiation produced by them is depleting the region and compressing the gas around them which leads to further star formation on the upper left side of the picture [16].

# 3 Active Galactic Nuclei

In observations since 1950s, several previously unobserved features of various objects appeared in multiple wavebands. Carl Seyfert was observing spirals at visual wavelengths and discovered galaxies with luminous nuclei and specific spectra. At the same time, radio astronomers discovered galaxies lying in between two bright radio sources. The presence of the synchrotron radiation and the shape of the radio lobes showed that they are created by powerful jets coming from the nucleus of the central galaxy. In 1950s, quasi-stellar objects - quasars - were discovered. They appeared point-like as stars at visual wavelengths but as distant galaxies by their redshift [11]. Nowadays, we assume that all these phenomena are explained by the presence of the accreting supermassive black hole in the center of galaxies, because, as can be determined from characteristics of the spectra, the source of the energy is convincingly non-stellar.

Galaxies with the accreting massive black holes are called *active* and the compact region producing the tremendous amount of energy *active galactic nucleus* (AGN). Such a nucleus has an excess in emission in many wavebands as can be seen in Figure 3.1.

We distinguish several types of AGNs. In some cases, the classification is to some extent artificial and follows the historic development of the field. In reality, some different types of AGNs describe the same object observed from different angle, as explained later. However, in other cases, AGNs physically differ. The most common AGNs are Type 1 and Type 2 Seyfert galaxies, quasars and radio galaxies. It is also possible to divide them according to the significance of their radio emission. AGNs, in which the radio band emission is dominated by the jets and radio lobes, are called *radio-loud*. If the jet-related emission can be neglected, we talk about *radio-quiet* AGNs. The former involve by definition radio galaxies, the later involve Seyfert galaxies. Quasars can be both radio-loud and -quiet.

The accepted model states that while matter is flowing into the central black hole, due to the angular momentum conservation, a flat disk is formed. The matter is accelerating and colliding and as a consequence, it produces thermal energy. Further from the central black hole, the accretion disk becomes thicker and cooler. Even further out, a dusty cool torus is formed [11]. The presence of the relativistic jets is closely related to the presence of magnetic fields, but is not yet entirely understood. Subsequently, the jets can form more distant structures through interaction with the surrounding material, like radio lobes [9].

The inner part of the disk emits X-rays and UV photons because of the extreme temperatures inside it. The velocity of the material causes large Doppler shifts, so
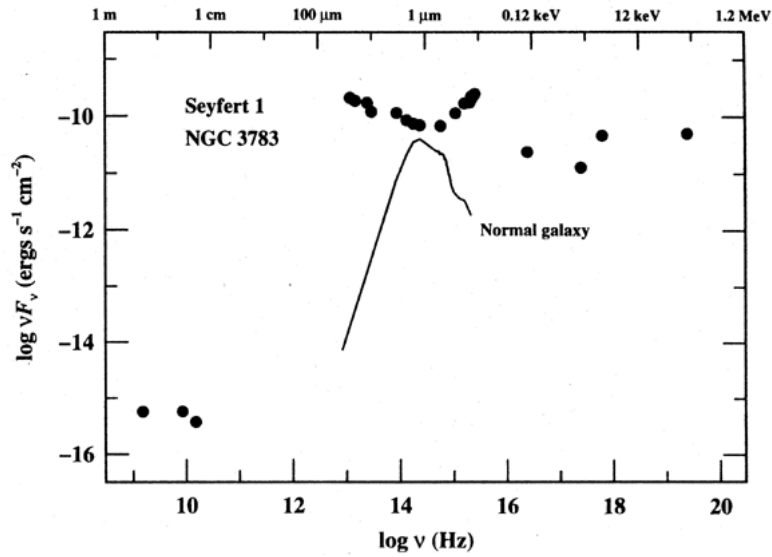
Fig. 3.1. The comparison of spectra of AGN and a normal galaxy. It is clear that the AGN spectrum has an excess in all wavebands, especially at the highest energies [17].

that the spectra of the galaxy observed from a suitable angle will have broad emission lines. However, if the sight is blocked by the dusty torus, only the gas under and above it is contributing to the spectra. Because this gas is more distant from the accreting black hole, it is not so fast and the emission lines are therefore narrower [11]. The former case is called Type 1 Seyfert galaxy, the latter Type 2 Seyfert galaxy. The *broad line region* contains gas clouds with density $n \gtrsim 10^{10}$ atoms/cm$^3$. The cloud structure is obvious from the presence of long-wavelength continuum radiation that would be absorbed within the evenly distributed gas. It is clear that the broad emission lines come from many different clouds present in the vicinity of the nucleus. On the other hand, the narrow spectra containing forbidden transition lines cannot originate from dense regions. From the Table 2.1 it is clear that the density of the *narrow line region* must be $n \lesssim 10^8$ cm$^{-3}$, otherwise the collisional de-excitation would dominate. The velocities that correspond to the width of the observed lines are about 10 times smaller than that of the broad line region, approximately 1000 km s$^{-1}$. The size of the narrow line region is usually a few kpc, but can be as extent as several hundreds kpc.

If the nucleus is very bright - brighter than the host galaxy itself - the object is classified as a quasar. In addition, if the synchrotron radiation from the jet in radio band is observed - the galaxy is radio-loud - the same distinction is used and the objects are called *broad* and *narrow radio galaxy*. If the jets are present and observed face-on, we talk about a *blazar*. This distinction is clarified in Figure 3.2.

## 3.1 Seyfert Galaxies

Seyfert galaxies contain emission lines broadened by large Doppler shifts. The width of the lines suggests that the velocities at the center of Seyfert galaxies are
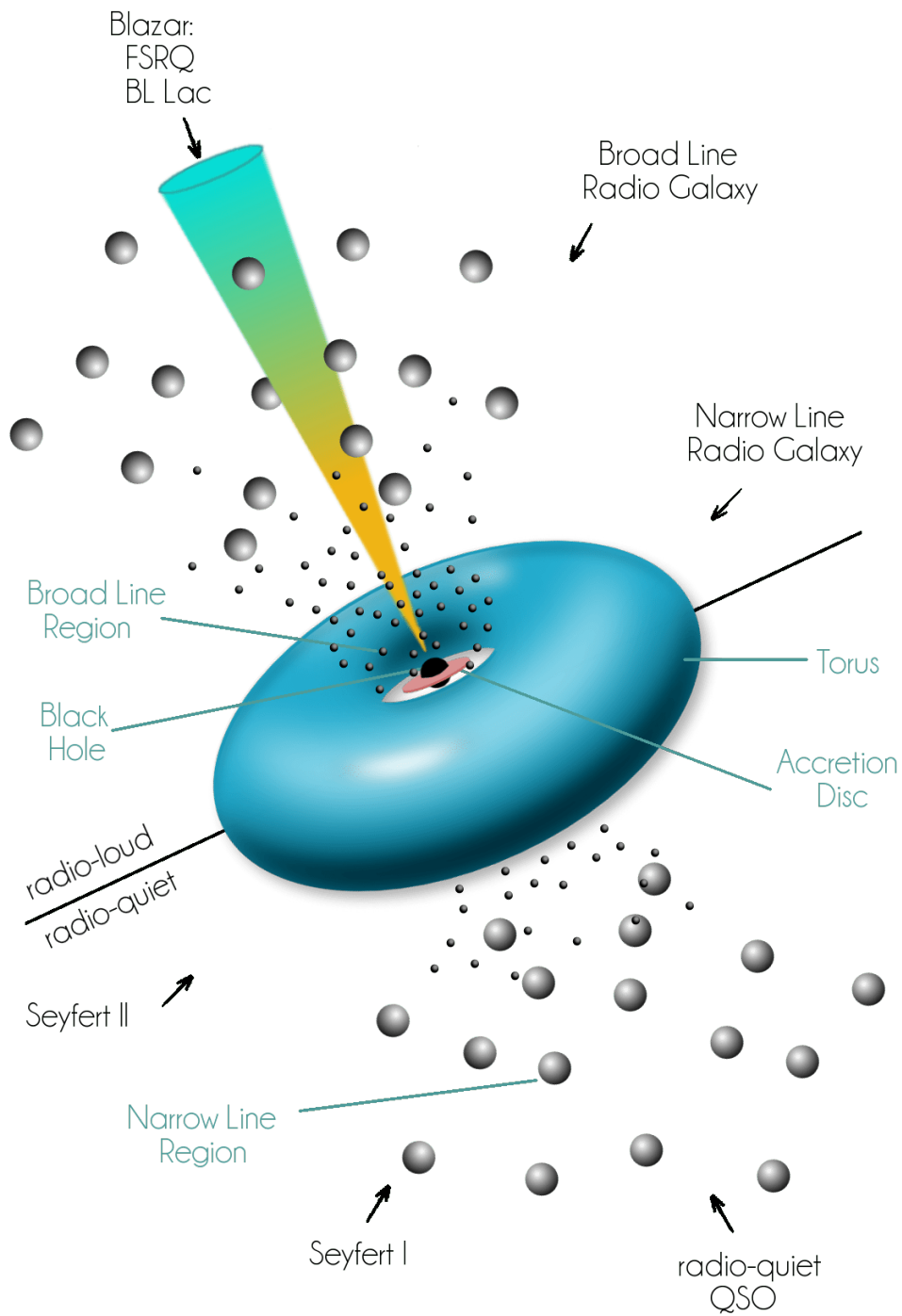
Fig. 3.2. The scheme of the Unified Model of AGNs. The upper part of the picture shows a galactic nucleus with the jet, therefore it is radio-loud. The bottom part shows the radio-quiet galaxies. For both cases, the origin of the broad and narrow line spectra is explained. In addition, both radio-loud and radio-quiet quasars are depicted, as well as the jet-facing blazar [18].

about 30  times greater than the velocities at the center of normal galaxies - in the order of 10 000 km s$^{-1}$ [11]. Moreover, the X-ray brightness of the nuclei can change within minutes. This implies that the diameter of the nuclei is only a few light-minutes, nonetheless the energy emitted by the nuclei is two orders of magnitude larger than the energy of the entire Milky Way. Approximately 2% of all spirals are Seyfert galaxies, so the presence of active nuclei is quite rare. As mentioned previously, they can be further divided into Type 1 and Type 2 Seyfert galaxies according to their spectra. Type 1 Seyferts have broad emission lines with narrow cores and are very luminous at X-ray and UV wavelengths. On the other hand, Type 2 galaxies are more quiet at the shortest wavelengths and their spectra show only the narrow line features. The classification of these sources depends on varying observing angle of the central black hole [11].

Usually, Seyfert galaxies are not strong radio emitters. Also, the luminosity drops for energies above about 100 keV which corresponds to $\gamma$-rays. The radio emission and some of the IR photons come from the relativistic jets. Within the jet, photons can be energized via scattering by electrons to $\gamma$-ray energies. The X-ray and UV radiation come from the inner part of the disk, if observable. The visible light probably originates further out. Moreover, the surrounding dust also emits in the IR.

The supermassive black hole has apparently a limit on luminosity that is sustainable with respect to the further infall of material. The pressure of the emitted photons can be so large that it causes an outflow of the material being accreted. Eventually, the black hole runs out of the material and the accretion shuts down. The limit is called the *Eddington luminosity* and is equal to

$$L_E = 3 \times 10^4 \frac{M}{M_\odot} L_\odot, \tag{3.1}$$

where the L$_\odot$ and M$_\odot$ are the luminosity and the mass of the Sun and $M$ is the mass of the central object [9]. The relation gives us the minimal mass of the black hole that will be able to gravitationally contra-balance the radiation-driven outflow for a given luminosity.

## 3.2 Quasars

The reason behind the initial confusion whether quasars are stellar objects or galaxies was that their luminosity is 10 to 1000 times larger than that of a common large galaxy, resembling Galactic stars, but the redshift suggested that the sources are actually distant [11]. Similarly to Seyferts, from the fluctuations in the brightness it is clear that the size of the very luminous source is only a few light-hours. Firstly, only radio-loud quasars were observed. Subsequently, during a search for objects resembling stars but emitting strongly in IR and UV bands, also radio-quiet quasars were discovered. Later it was revealed that the sources are surrounded by normal-feature spectra, meaning that they are located at the center of galaxies but they are so bright that they outshine the stars in it [11]. Quasars are considered to be a more powerful version of the Seyfert nuclei [9].
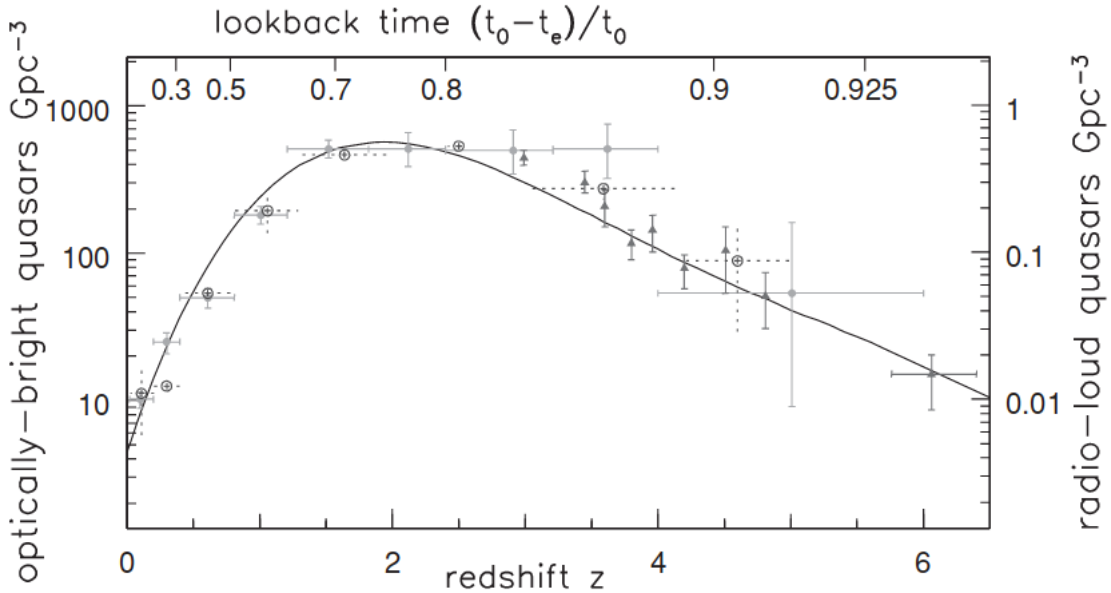
Fig. 3.3. The density of radio-loud quasars as a function of the redshift and the look-back time, respectively. The triangles show optically bright quasars, the filled dots show quasars bright in soft X-rays and the open dots in hard X-rays [9].

Thanks to their brightness, it is possible to detect $z > 6$ quasars. That provides an important insight into the spectra of objects with a large variety of ages. Surprisingly, the spectra do not significantly differ in the relative abundance of elements. That means that already approximately 1 Gyr after the Big Bang, the first generation of stars already enriched the galaxy nuclei in heavy elements. The distribution of quasars with respect to the redshift peaks at $z \sim 2$ (Figure 3.3), when their abundance was 30 - 100 times larger compared to present. This phenomena can be explained by the mechanism of the black hole activity triggering described bellow.

About 99% of quasars are radio-quiet. The radio-loud quasars are, on the other hand, one or two orders of magnitude stronger radio emitters than typical radio galaxies.

## ▍ 3.3 Radio Galaxies

All types of AGN exceed the normal galaxies in the radio band luminosity − Seyfert galaxies' radio luminosity is 100 - 1000 times larger and in radio galaxies, the luminosity is $\sim 10^8$ - $10^{12}$ $L_\odot$ [9]. The source of the polarized radio emission is the synchrotron radiation produced by electrons spiralling along the magnetic fields in the relativistic jets [11]. These jets channel the energy to the radio lobes that are located on both sides of the galaxy and their size is proportional to the power of the jets. The lobes, possibly as large as 3 Mpc, are also an additional source of the synchrotron radiation of the radio wavelengths. Jets can be both one- and two-sided. Inside them, electrons must be accelerated to high energies to be

able to produce synchrotron radiation with short wavelengths such as X-rays. From the life-time of electrons in these conditions, it is clear that their origin is not in the nucleus of the radio source. The acceleration presumably takes place in the shock waves in the jet. Radio galaxies are usually elliptical unlike the Seyfert galaxies that favour spirals.

## 3.4 Triggering the AGN activity

The majority of observed galaxies have a supermassive black hole in their centres but only a few percent of them are active. The process of the AGN triggering resembles the ignition of the star formation activity. In order to trigger the black hole to accrete matter, cold gas needs to be present in the galactic center. This resemblance is supported by the AGN activity and star formation correlations. The AGN activity is considered a phase of galaxy evolution that can be entered via interaction with other galaxies in the cluster that influences the gas content in them. Observations support the theory that AGN is triggered by merging of galaxies as well as a ram pressure invoked by their close passing. The ram pressure is known to cause a cold gas depletion in some cases which leads to formation of gaseous tails behind the galaxy moving through the inter-cluster medium. However, the same pressure can also cause the gas compression and subsequent ignition of the star formation and the AGN activity [19]. Many observed AGNs lay in distorted galaxies with a companion implying it could have been the remnant of their passed interaction. In other cases, the AGN seems to orbit an object with similar mass, that could be another supermassive black hole from the merged galaxy [11]. Both processes are highly dependent on the position of the galaxy within the cluster [19]. The connection between interactions of galaxies and the AGN activity explains the distribution of AGN through the history of the Universe - the population dependence on the redshift. At the largest redshifts, the Universe was so young that not many galaxies were already formed so that their interactions were rare. The distribution peaks at z of around 2 - 3, when there were galaxies present but the Universe was not yet very expanded. The rate of the merging was approximately 3 merging events for each galaxy per $10^9$ yr. At this time, quasars were 1000 times more common than in the Local Universe [11]. In the context of the galaxy evolution, the AGN formation seems to be bound to the formation of the central bulge but not the disk. The masses of the black hole and the bulge are connected through the $m_{\mathrm{BH}} - m_{\mathrm{bulge}}$ relation studied by many works [20], [21], whilst no correlation was observed for the disk mass [22].

## 3.5 The Matter Accretion

The physics of the accretion disk revolves around the angular momentum conservation. The angular momentum $L = mvr$ prevents the matter from falling directly onto the massive object that it is being attracted to and causes the formation of the flat disk within which are the individual particles orbiting the

object on approximately circular paths [23]. In order to make the matter fall into the black hole, the angular moment needs to be lost [24]. The sum of the individual angular momenta, the total $L$ of the disk, is conserved via its transport or redistribution. Specifically, the angular momentum is transported from the inner regions of the disk to the outer ones, allowing the matter to fall in. The way this is achieved is tightly bound to the presence of magnetic fields in the ionized gas [25]. Two particles orbiting the black hole on two different orbits have different velocities (the inner orbits have higher velocities) and also angular momenta. If they are bound by a weak magnetic field, the faster particle is speeding the slower particle up, reducing its own angular momentum. As a consequence, it needs to decrease to a lower orbit and gains speed. The second particle does the opposite and as a result of the angular momentum increase, it moves to more distant orbit and slows down [26].

Besides this effect, the transformation of the gravitational potential to the thermal radiation is ongoing in the same way as in the collapse of the gas cloud during the star formation.

The overall effect is that up to 10% of the rest mass of the accreted matter is released in the form of radiation [9].

# 3.6 [OIII] Emission Line

The importance of the [OIII] emission line lays in the fact that it can be used to estimate the AGN bolometric luminosity and also to define the size of the narrow line region. Specifically, the [OIII] 5007Å line is used for this purpose. It originates from the ionization of the gas in the narrow-line region by the ionizing radiation that escapes the dusty torus obscuring the supermassive black hole along its polar axis. This emission line is easily detected and suffers from less attenuating effects than the lines coming from regions closer to the supermassive black hole [27]. The [OIII] 5007Å is not the only possible AGN luminosity proxy. The [OIV] 25.9 μm and [NeV]14.3,24.3 μm emission lines originate from the same ionizing process within the NLR. However, since they are mid-IR lines, they almost do not suffer from the dust attenuation and their ionization potential lays in the band where hot stars do not produce much radiation. On the other hand, they are less abundant and therefore more challenging to observe. The [OIII] 5007Å has been observed at hundreds of thousands of targets, so that the high statistics speaks in its favour. Besides the NLR lines, the mid-IR continuum coming from the warm dust in the torus and the X-ray emission directly from the black hole can be used. The [OIII] emission line still needs to undergo a correction for the dust attenuation by the so-called Balmer decrement [27]. The exact relation between the AGN luminosity and the [OIII] luminosity - the bolometric correction - is empirical and differs in the literature. Heckman [28] used the correction by the factor of 3500 for the raw $L_{\mathrm{OIII}}$, while Kauffmann and Heckman [29] used the correction of 600 for the extinction-corrected $L_{\mathrm{OIII}}^{\mathrm{c}}$.

The other role of the [OIII] emission line is the definition of the size of the NLR. However, the definition also varies. The most straightforward method is to adopt

the maximum $3\sigma$ detected radius of the [OIII] line as the size of the NLR. However, the result from this method depends on the sensitivity limit of the used instrument. Therefore, it is more reliable to use the definition based on a specific [OIII] surface brightness isophote. Of course, this method is a subject of the choice of the surface brightness threshold. In Liu et al. [30], the threshold is set to $10^{-15}$ erg s$^{-1}$ cm$^{-2}$ arcsec$^{-2}$ usable for studies of quasars. In Chen et al. [31], the threshold is $10^{-16}$ erg s$^{-1}$ cm$^{-2}$ arcsec$^{-2}$. The used argumentation is such that the value is reached by the majority of the AGN-flagged spaxels of the targets that the study focused on. Because the sample of this thesis is a sub-sample of the Chen et al., the same threshold of the NLR size was adopted.

One of the drawbacks of using the [OIII] emission line to map the vicinity of the supermassive black hole is the fact that the imposed ionizing radiation can come from the AGN as well as from the newly-formed stars. Luckily, there is a way how to distinguish between the two. The hard continuum from the AGN and the much softer O-star continuum cause different ionization of the gas that they reach. The origin of the given ionized gas can be determined by the ratio of the forbidden and allowed emission lines using the so-called *BPT diagram.* Firstly introduced by Baldwin et al. (1981) [32], the diagram compares the ratios of the [OIII] 5007Å/H$_\beta$ and [NII]6584Å/H$_\alpha$, [SII]6716,6731Å/H$_\alpha$ respectively. With an additional classification by Kewley et al. [33], it is capable of a distinction between star-forming galaxies, composite active galactic nucleus-HII (AGN-HII) galaxies, Seyferts and LINERs[1]. However, there is no combination of emission lines that provides a reliable distinction between all kinds. Different line ratios are sensitive to different physical properties of the studied regions. Generally, the hard continuum of the AGN leads to a greater photoionization heating and the subsequent higher temperatures cause a larger abundance of forbidden lines coming from collisional excitation [27]. In this thesis, the diagnostics using both NII and SII BPT diagrams is used and compared.

---

[1]LINER - a low ionization nuclear emission-line region - is another type of AGN. The "low ionization"refers to the fact that the spectrum of this AGN contains emission lines predominantly from weakly ionized atoms.

# 4 Integral Field Spectroscopy

Integral Field Spectroscopy (IFS) offers an opportunity to peer inside observed objects by providing many different spectra for the same target while maintaining their spatial information. The basic principle is explained in Figure 4.1.
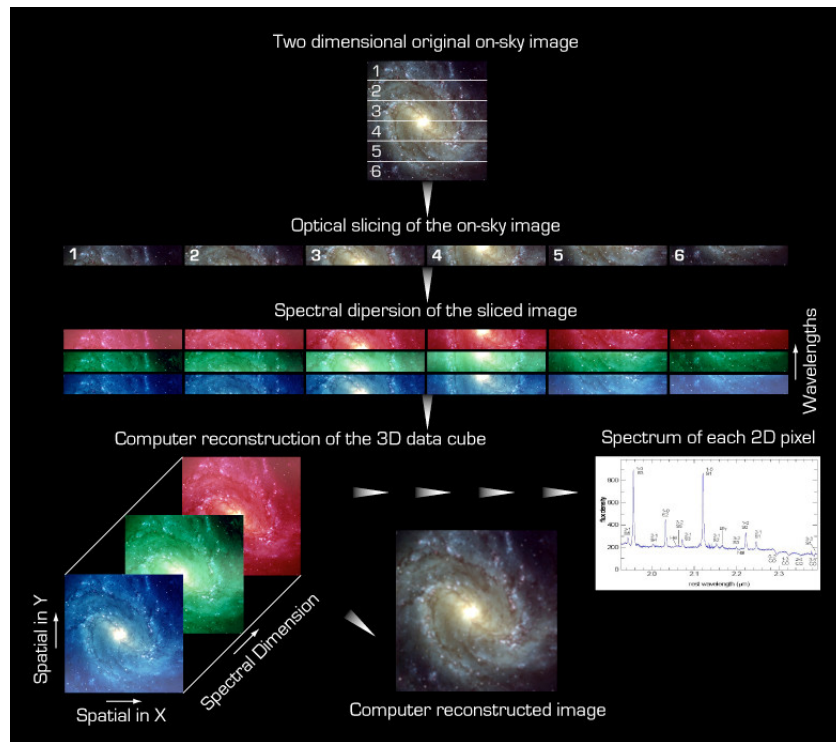


Fig. 4.1. The basic principle of the IFS. The on-sky image is firstly divided using one of the techniques described below. Then, each individual segment of the original picture is dispersed. Subsequently, a full image is reconstructed from the dispersed segments for each wavelength. The result is a 3D data cube consisting of two spatial coordinates and one spectral coordinate in which the spectra of individual pixels are stored [34].

To study the AGN feedback mechanism, as well as many different galaxy properties, spatially resolved data are priceless. The spatial distribution of emission lines alongside other properties can trace the star formation sites, which help us with the overall understanding of galaxy evolution. Stellar ages and element abundances are leads of the galaxy disk growth. Last but not least,
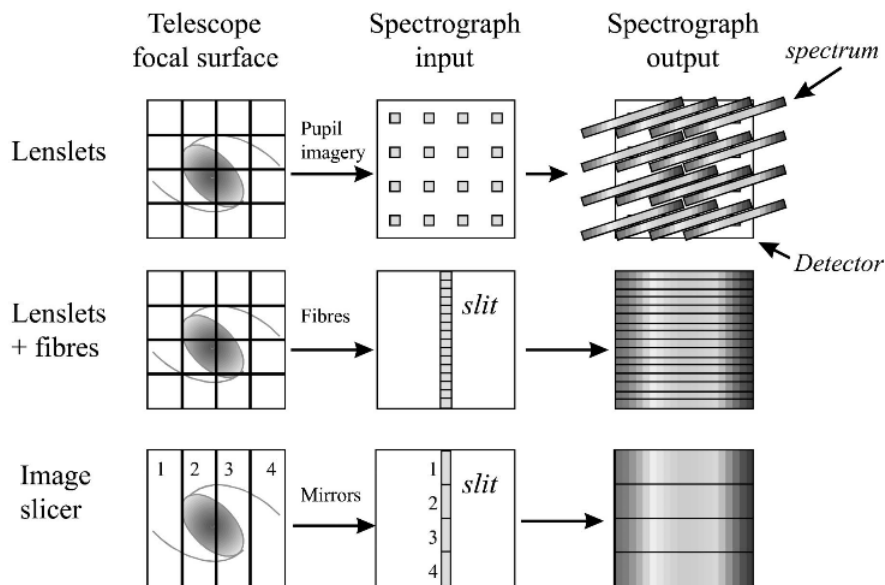
Fig. 4.2. The scheme of three different IFS techniques. The first column shows different ways of the original image segmentation and the subsequent transmission to the spectrograph. The second and third column show the spectrograph input and output, respectively, clearly illustrating the differences in detector efficiency [34].

revealed two-dimensional dynamics carries information about baryonic interactions with host dark matter halos through the angular momentum distribution [35]. Although there have been successful spectroscopic surveys before spatially resolved image spectroscopy, they suffer from a drawback of being possibly biased by the limited area of the object that can be observed at the same time. That can cause a loss of valuable information of internal galactic processes.

To provide a three-dimensional data cube consisting of two coordinates and a spectral information in the third dimension, two different approaches can be engaged. Either each target is gradually scanned or the IFS is used [36]. The scanning techniques (e.g. frequently used long-slit spectroscopy stepping in the spatial coordinates and Fabry-Perot interferometry stepping in the wavelength space [36]) require additional time and suffer from atmospheric fluctuations during the scan, whereas IFS is providing the 3D image continuously [37]. For this reason, the majority of new large telescopes are equipped with integral field units (IFUs). There are three main techniques of IFS that differ in the way how the original image is segmented and fed to the spectrograph as is shown in Figure 4.2 [38]. The first technique uses a microlens array (MLA). The original field is divided by the MLA and is transformed into a pupil image. The pupil image is subsequently processed by a spectrograph providing spectrum of each pupil. Because of the two-dimensional arrangement of pupils, the dispersion direction needs to be adjusted to prevent overlaps as can be seen in Figure 4.2. This results in a presence of gaps in between the spectra that lowers the efficiency of the detector. Moreover, the needed adjustment of the dispersion direction constraints the length of the spectra. For this reason, the technique is suitable for such experiments that

do not require long spectra [38].

To deal with the potential overlap problem, fibres can be used to rearrange the image to a one-dimensional slit that enters the spectrograph. A disadvantage of this approach is a loss of data due to inactive parts of the fibre such as cladding. This can be overcome by usage of microlens array at the input that focuses the original image directly into the core of the fibre. Such a system requires high precision of the MLA placement to avoid a data loss in the transmission between the lenslet and the fibre [37].

For experiments where cryogenics has to be used in order to reduce the thermal background, image slicer can be employed. The image created by telescope is divided by segmented mirror, each slice of which is arranged in a slightly different angle. The resulting input of the spectrograph is a slit within which individual slices are ordered end to end. An advantage of such a system, besides the potential usage of cryogenics, is that the unavoidable diffraction affects only one dimension in contrast with the previous methods. However, the manufacturing of an image slicer is challenging and remains the main constraint of its usage even though the concept originated as early as 1938 [37].

## 4.1 IFS Surveys Overview

Starting in the 1990s, IFS has become an irreplaceable observation technique. A short overview of the chosen IFS surveys follows.

Multi-slit or multi-fibre spectrographs have been used even before the IFS for multi-object spectroscopy (MOS). To use the telescope time and capacity efficiently, these complex spectrographs have been engaged to record spectra of many targets at the same time [39]. Even though the idea of fibre-fed spectrograph originated in early 1970s, the technical challenges of the technology were overcome almost 10 years later when the MEDUSA experiment performed the first multiobject observations [40]. First multi-slit data were recorded in 1982 using a 4-meter telescope at the Kitt Peak National Observatory in Arizona [39].

The first 3D system was a scanning Fabry-Perot spectrograph whose first light came in 1974. The history of IFS starts around 1980 as the first technique to obtain the full spatio-spectral coverage in a single exposure. The three of the currently most common approaches started to evolve around the same time, delivering MLA-based TIGER in 1989, fibre-based SILFID only one year later and, finally, SPIFFI in 1993, whose integral field units were slicers [39]. SAURON spectrograph using the MLA started taking data in 1999. Among its prominent results is a classification of early-type galaxies according to their kinematics rather than morphology (E, S0) [41]. The DiskMass Survey studied mass-to-light ratios and mass profiles of star-forming spiral disk to shed a light on the shape of dark halos in the inner parts of the disk galaxies or tested the maximum-disk hypothesis [42]. The survey concluded that the most disk galaxies are submaximal[1] [35].

---

[1]Maximum-disk hypothesis studies the importance of the dark matter halo for the inner regions of the galaxy. If the mass of the disk is dominating, the galaxy is considered *maximal*. In *submaximal* galaxies, the dark matter halo is important [43].

The European Southern Observatory employs a number of IFS instruments. At the beginning of the millennium, fibre-based FLAMES (2002), VIMOS (2002), which combines MLA with fibre-bundles and image-slicing SINFONI (2004) started to operate. One of the scientific highlights of FLAMES is the discovery that the sodium content in stars suggests whether they reach asymptotic giant branch during their lifetime [44]. In 2017, VIMOS delivered a very exciting detection of the first light coming from the gravitational wave source - apparently a two neutron stars merger [45]. In the same year, SINFONI revealed that the early galaxies were more dominated by baryonic matter rather than dark matter as present-day galaxies. This discovery was made in the cooperation with other ESO instrument, KMOS - one of the most recent instruments installed on ESO's Very Large Telescope (VLT) - operating since 2012 [46]. Another second-generation VLT instrument is MUSE (2014). Both KMOS and MUSE are working on the principle of an image slicer. In 2017, MUSE completed the deepest spectroscopic survey ever made. Focusing on the Hubble Ultra Deep Field, MUSE studied 1600 very faint galaxies, discovering 72 new [47].

## 4.2 MaNGA

MaNGA (Mapping Nearby Galaxies at Apache Point Observatory) is an IFS survey and one of the major programs of the fourth-generation Sloan Digital Sky Survey (SDSS-IV) that began in 2014 and will be completed in 2020 [35].
The goal of the MaNGA is to study the internal structure and composition of 10 000 low-redshift galaxies. The wavelength coverage from near-UV to the near-IR (3600 - 10300 Å) and an unparalleled sample size promise to unveil the nature of processes that drive the galaxy evolution. Their physical origin is the MaNGA's main objective. These processes involve the gravitational collapse, star formation and its regulation through the feedback, merging with neighbouring galaxies and AGN accretion. MaNGA is not only trying to probe them individually but also connect all of these phenomena with the environment in which galaxies exist [35].

### 4.2.1 Science Goals

The key science questions of MaNGA are specifically [35]:

- What is the nature of growth of the galaxy disks and where does the gas needed for the growth originate from?

- How do stellar accretion and merging connect to present-day growth of galactic bulges and elliptical galaxies?

- What is the shut-down mechanism of galaxy star formation both internally and externally?

- What does mass and angular momentum distribution among different galaxy components look like?
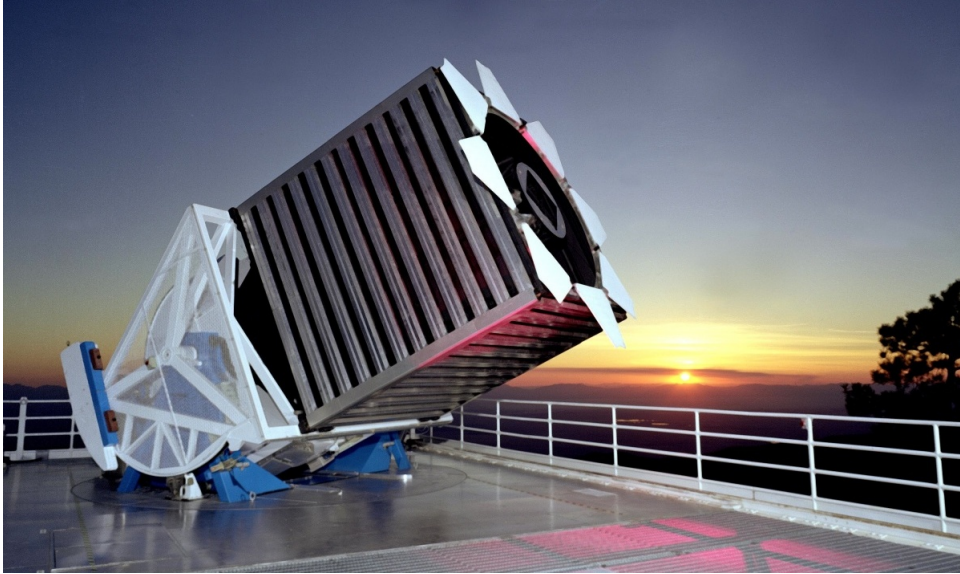
Fig. 4.3. Sloan Foundation 2.5-m Telescope at Apache Point Observatory, New Mexico [48].

After the completion later this year, MaNGA is believed to provide answers to these open questions of modern astrophysics. To approach the first two questions, MaNGA will provide spatially dependent star formation rate (SFR) and metallicity of the gas available in the galaxy and compare it to older stellar population to map the recent gas accretion. However, not only gas accretion and the subsequent star formation drive the disk growth. MaNGA will also probe the kinematics of mergers to shed a light on different merger phases and minor interactions that could explain the size growth observed in elliptical galaxies. Both phenomena will be then compared to models predicting the ratio of stars formed by different processes. MaNGA hopes to answer the questions of how much gas is formed in the galaxy internally and how much comes from the accretion [35]. However, merging can be also responsible for quenching star formation. To form new stars, there has to be a cold gas supply that can be acquired through both internal and external processes as discussed above. Mergers driving the inflow of cold gas can ignite central starbursts and fuel AGNs. Subsequently, starbursts consume the internal gas supply and the remaining gas is either heated or blown out by winds from the AGN or the starbursts itself. Like in the previous case, there are also external processes that can take part in the galaxy star formation quenching. If the galaxy is a part of a group or a cluster, tidal forces occurring due to the reciprocal movement with companion galaxy or their surrounding hot medium can be responsible for the internal gas heating which disables further star formation. MaNGA will exploit its near-UV resolution to probe specific spectral indices that evaluate the fraction of old and young stellar populations. Gradients in these diagnostic tools will hopefully provide a complex picture of the quenching process [35].

The third scientific goal is closely related to the galaxy formation history. The different channels of the formation leave their imprints in the mass and angular

momentum distributions. The main challenge of the decomposition of these channels lies in the unknown contributions of different galaxy constituents to the total mass caused among others by uncertainties in dark matter influence. MaNGA is believed to shed a light on this problem with its 2D mapping of stellar rotation and velocities dispersion as well as its long wavelength coverage [35].

## 4.2.2 Instrumentation

In this section, an overview of MaNGA instrumentation is provided. The MaNGA uses the Sloan Foundation 2.5-m Telescope at Apache Point Observatory, New Mexico (Figure 4.3), with the field of view of 3°. The connection between the fibres at the focal plane of the telescope and spectrograph is arranged using custom-made cartridges. Cartridges contain specially designed alluminium plates with 17 holes drilled in them. Each of the holes corresponds to one target and is filled with suitable fibre-bundle according to its size. In this way, MaNGA allows a simultaneous observation of 17 targets. The collected light is subsequently fed into two BOSS spectrographs [49]. The cartridge scheme can be found in Figure 4.4.
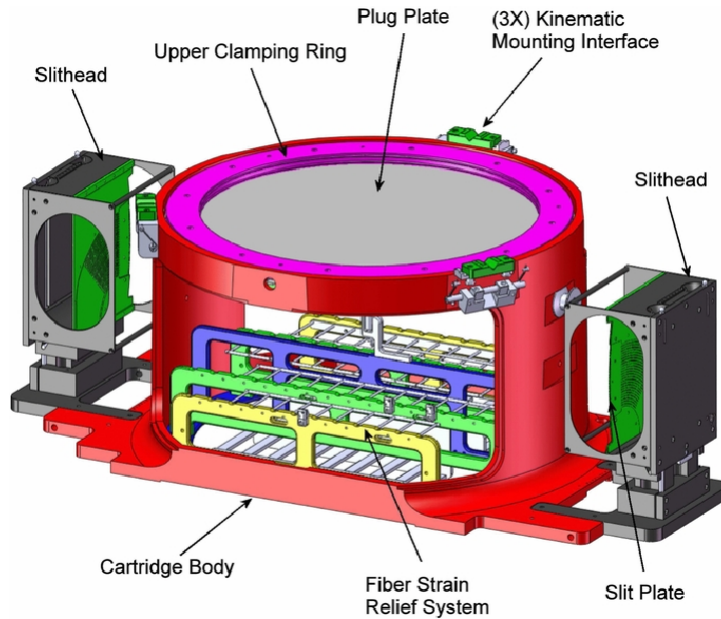


Fig. 4.4. The cartridge connecting the IFUs at the focal plane of the telescope and the spectrographs. It consists of an aluminium body that supports the fibre harness, two slit-heads, and the plug-plate with 17 holes for the individual targets. Each of the holes is filled with an IFU from the bottom [50].

Firstly, the reasoning behind the IFU design to match the scientific and observational requirements is described. The diameter of each IFU fibre is $\sim 2"$, which matches the typical ground-based seeing[2]. Taking into consideration the typical intrinsic size of target galaxies, which is approximately from 3 to 9 kpc, the

---

[2]"Seeing" (the FWHM of the point spread function) is the best achievable angular resolution for a given telescope. It corresponds to the size of a blurring resulting from observation of a point-like source through atmosphere [9].

spatial resolution requirement is then ∼1 kpc, so that even the smallest galaxy is covered by at least 3 radial bins. Based on these constraints, the physical spatial resolution is maximized by targeting galaxies at a redshift of 0.03.

The survey duration was estimated with respect to the desired sample size of 10 000 galaxies. The density of targets and the telescope field of view yield ideal arrangement of approximately 20 fibre-bundle IFUs on 500 different pointings (plates). Considering the weather conditions, dark time and time sharing with other Sloan surveys, the required time was estimated to be 6 years.

The number of fibres per IFU needed was derived from the typical optical radius of z ∼ 0.03 galaxies of 10". Taking into consideration the size of the fibre of 2" and the used hexagonal geometry of the bundles, the number of fibres of 61 per IFU is derived. However, the survey can not use a single arrangement of IFUs based on this estimate. One of the MaNGA's strongest features is the statistics of the unprecedented sample of 10 000 targets. To study galaxy properties as a function of the effective radius $R_e$, uniform coverage is needed. To follow the variance of the $R_e$, the number of fibres per IFU should also vary in size. This requirement is impossible to fulfill because the size range of the IFUs would have to extent over two orders of magnitude. For this reason, the target selection was adjusted so that the apparent angular size does not change a lot among targets, meaning that the intrinsically largest galaxies are observed at higher redshifts. The final redshift range of the survey is therefore of 0.03 < z < 0.1 [35].
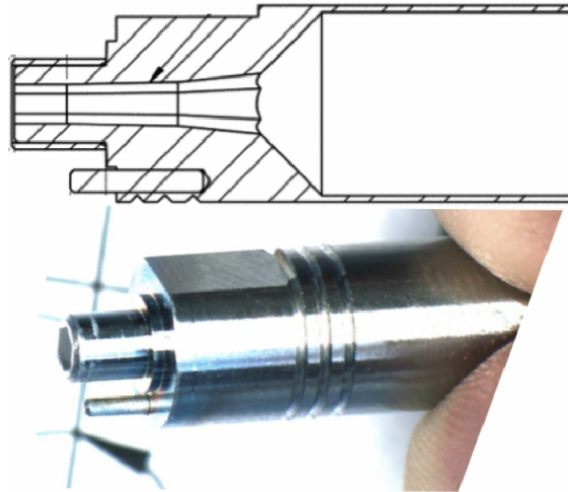


Fig. 4.5. IFU ferrule scheme and picture. The scheme shows the transformation of the ferrule shape from the wide circle for easy plug-in to the desired hexagon. The final shape is visible in the bottom picture showing the IFU to be plugged into the plate of the cartridge [35].

### Fibre-bundle Integral Field Units

MaNGA collaboration's objective was to create an universal, inexpensive design, because of the large number of different IFUs required. The range of bundle sizes extents from 19 to 127 fibres. To keep the fibre in place with high precision, but

also to make the manipulation as easy as possible, a special ferrule housing was designed. The inner hole has a shape such that it is possible to insert the bundle by hand and it subsequently transforms into the desired hexagonal shape, rearranging fibres into their final position. This process leads to only ∼3 μm shift from perfect hexagon on average, which can be compared to the fibre core size of 120 μm [49]. The fibre-bundle then leads to the pseudo-slit of the spectrograph. The connection is provided by the V-groove blocks of 21-39 fibres fanned out to one row. These blocks are then directly connected to the slit-head of the spectrographs. The position of individual fibres in the block is chosen to minimize the impact of cross talk on the CCD detectors [35]. Such mapping from the fibres' original position onto the position in the block is shown in Figure 4.6. Each of the spectrographs contains 22 V-groove blocks yielding the total number of 1423 fibres [51]. The fill factor of the IFUs is 56%. Other fibre-based IFU survey that MaNGA adopted the IFU design from, SAMI, reaches the fill factor of about 75%. However, the fabrication of the IFUs is considerably more complicated and expensive [35].
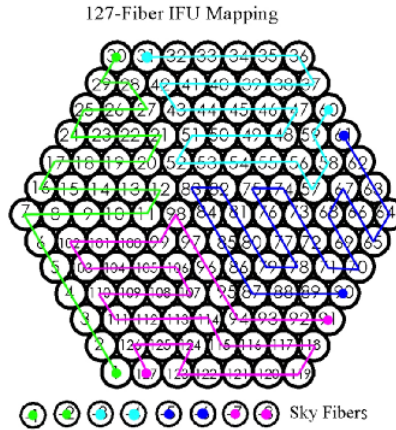


Fig. 4.6. Mapping of fibres from the largest MaNGA IFU in the telescope focal surface to the spectrograph slit. Different colors trace fibres mapped into different V-groove blocks [49].

## BOSS spectrographs

To cover the wavelengths from near-UV to near-IR, each of the two identical spectrographs is equipped with red and blue arm. The input of both spectrographs is aligned with the slit heads placed on the body of the cartridge. The beam entering the spectrograph after collimation is split at 605 nm to red and blue channel. The subsequent instrumentation - a camera, CCDs and a grating prism - is then channel specific. The resulting spectral resolution $R = \frac{\lambda}{\Delta\lambda}$ is different for each channel. The resolution of $R \sim 2600$ at 9000 Å is reached on the red side. A $R \sim 1400$ is reached on the blue side at 4000 Å[35].

The CCDs have dimensions of $4000 \times 4000$ pixels with a pixel size of 15 μm. The projected spectrum has the spatial FWHM of 2.3 pixels. The read-out time is 70 s [35].
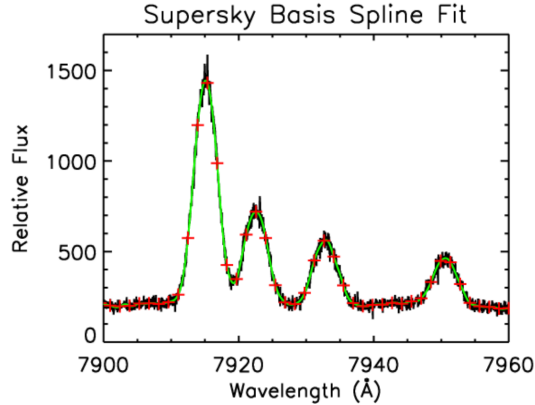
Fig. 4.7. The detail of OH-emission-dominated wavelength region of the sky spectrum from combined individual sky fibres. The red points represent the model, the black line the real data and the green line their fit [54].

### ◼ 4.2.3 MaNGA Data

MaNGA is an IFU survey, meaning that its data product is a 3D datacube. Data are already sky-subtracted and spectrophotometrically calibrated. MaNGA engages two different pipelines to provide the users convenient way of working with the data - Data Reduction and Data Analysis Pipeline (DRP and DAP, respectively). The whole six-year-long survey is expected to collect ∼100 million raw-frame spectra and ∼10 million reduced spectra.

The Data Reduction Pipeline (Figure 4.8) contains the individual fibre spectra in its 2D stage and subsequently combines them to a complete datacube in the 3D stage. The 2D stage is based on the reduction pipeline of the BOSS spectrographs and its goal is to produce the spectra for each fibre from the raw CCD data. The 3D stage is custom-build for MaNGA only, but follows reduction pipelines of other IFU surveys, such as CALIFA whose data reduction pipeline is described by Husemann [52]. Even before the spectra are extracted from the CCD, frames are preprocessed e.g. by removing the overscan regions[3]. Then, all calibration exposures are processed. Each exposure contains several bundles for other than scientific purposes - individual sky fibres for the sky subtraction and seven-fibre minibundles that are targeting standard stars for the flux calibration. The combined sky fibres are used to create a model of the sky spectrum (Figure 4.7) that is subsequently subtracted from all scientific fibres.

The minibundles provide the exposure-specific flux calibration vector. The product of the 2D stage is a FITS file[4] for each exposure that contains row-stacked spectra (RSS). The file is organized as a two-dimensional array, where each row is a one-dimensional spectrum of each of the 1423 fibres. The spectra have a common wavelength grid to which are interpolated from the 4 detectors. When the desired number of exposures is reached, the 3D stage of DRP is triggered. The algorithm identifies the relevant spectra among the individual FITS files and combines them

---

[3]Overscan region is a set of pixels used to measure the average signal introduced by CCD read-out. Their value - the bulk offset - is subsequently subtracted from all pixels [53].

[4]Flexible Image Transport System (FITS) is a file format commonly used in astronomy.

to the complete datacube. Each datacube contains a bitmask for both 2D and 3D stage of the DRP to provide a quality control. This is important for detection the problematic pixels that should not be used for scientific purposes for multiple reasons such as cosmic ray events, missing fibres and bad weather conditions [51].
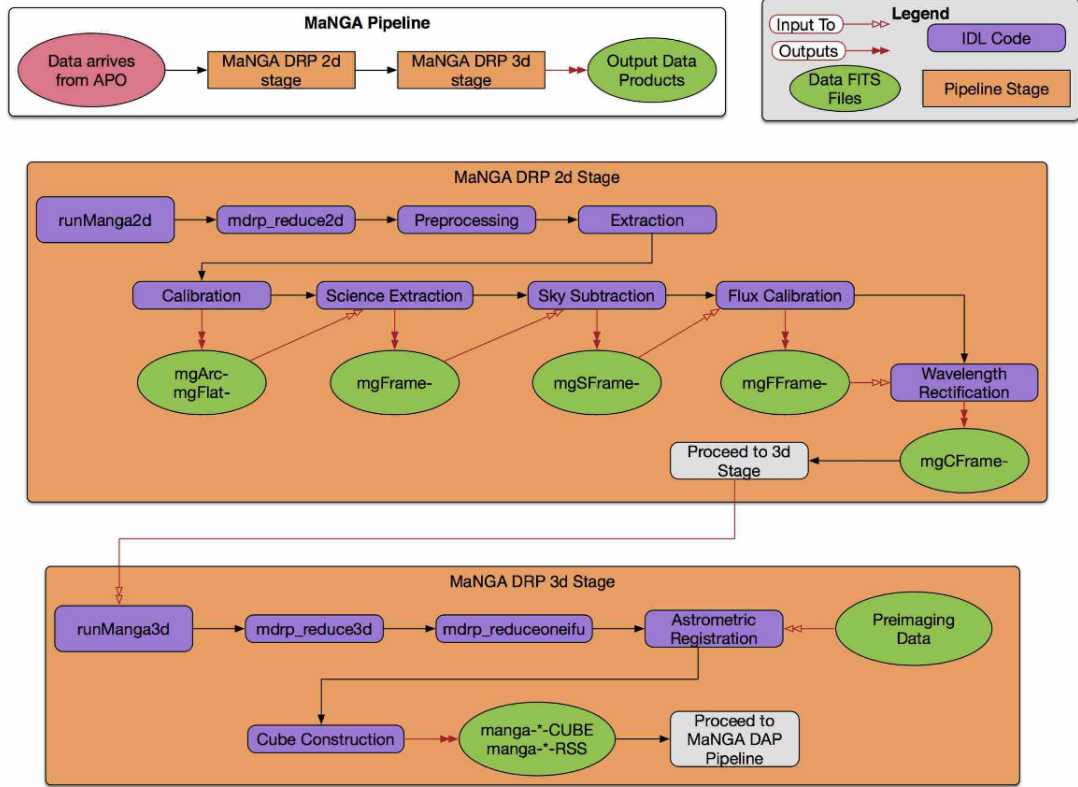


Fig. 4.8. The schematic overview of the DRP. The upper white box presents the basic pipeline sequence. The orange boxes then show the 2D and 3D stages of DRP in detail [51].

The final product of the DRP is the input of the Data Analysis Pipeline, which derives some important properties of the targets that can be immediately used for scientific objectives of users. The examples of such properties are shown in Figure 4.9. The spatial dimensions of the DAP and DRP outcomes match. These images are called *maps* and can be displayed with a MaNGA tool Marvin (see Cherinka [55]) that has both a web interface and a Python package to be implemented by users to their analysis. Similarly to DRP, DAP has its own quality evaluation. For this reasons, some pixels are masked from the map, as can be seen in Figure 4.9. It is important to note that the physical diameter of the fibre is larger than the sub-sampled spatial pixels (spaxels) on the map. The FWHM of the point-spread function is 2.5 arcsec while the spaxel size is $0.5 \times 0.5$ arcsec. This leads to covariance between the spaxels that needs to be treated carefully when the data is interpreted. More on this topic can be found in Westfall et al. [56].
In this thesis, several Marvin tools were used - mainly the [OIII] flux map from the DAP and the BPT Diagram-diagnostics for the masking of other-than-AGN spaxels of each map.
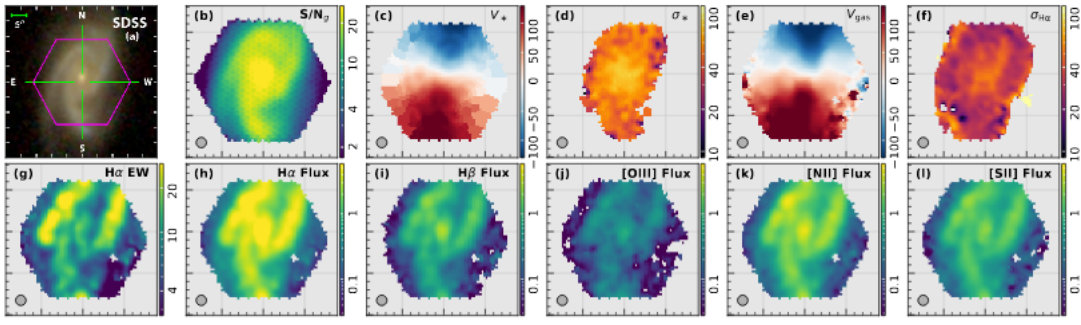
Fig. 4.9. The example of the products of DAP. From the top-to-bottom and left-to-right: (a) shows the SDSS image of the MaNGA target 1-605884 with the size of the IFU outlined in purple, (b) $g$-band[5]signal-to-noise ratio, (c) stellar velocity, (d) stellar velocity dispersion, (e) ionised-gas velocity, (f) velocity dispersion of the H$\alpha$ emission line, (g) the equivalent width of the H$\alpha$ emission line, (h) the flux of the H$\alpha$ emission line, (i) the flux of the H$\beta$ emission line, (j) the total flux of the [OIII] emission lines, (k) the total flux of the NII emission lines and (l) the total flux of the SII emission lines [56].

## 4.3 MASCOT

The MaNGA-ARO Survey of CO Targets (MASCOT), providing data for the analysis in this thesis, is a survey combining the data from MaNGA survey described in Section 4.2 that covers an extended optical band, and radio data from Arizona Radio Observatory (ARO).

The MASCOT sample is being assembled within two programs at ARO as part of the MASCOT 1.0 and MASCOT 2.0 programs. The ARO telescope, a former AEM ALMA prototype antenna, was given to the University of Arizona to install it on Kitt Peak. As a part of this agreement, ESO was granted a total of 3600 hours from 2015 to 2020 of observing time which was distributed among multiple projects. This time was dedicated to large scale Public Surveys such as MASCOT which was chosen to be one of them.

The pilot MASCOT 1.0 survey was granted 200 hours at ARO in 2018 and observed 34 sources from the MaNGA targets. The sample selection was done using the then available Data Release 14 [58] containing 2778 galaxies at $0.01 < z < 0.15$ with a mean $z \sim 0.05$. The follow-up MASCOT 2.0 survey is currently ongoing and targeting 150 MaNGA galaxies within 1200 hours that it was awarded. Sources have been selected from MaNGA Data Release 15 [59]. The total sample of almost 200 galaxies is large enough to draw statistically significant conclusions about some key galaxy evolution questions.

The goal of MASCOT observations is to map the molecular gas via the $^{12}$CO(1$\rightarrow$0) emission line in these targets that are, thanks to the MaNGA observations, spatially resolved. Therefore, it is possible to combine the sophisticated IFU diagnostics that MaNGA provides with the molecular gas information from ARO.

---

[5]Bandpasses, such as g-band, are engaged to specify characteristics of the instrument for a given wavelength range. An effective wavelength midpoint of g-band standar filter is 464 nm [57].

The Arizona Radio Observatory currently operates two telescopes. A 12-meter Telescope that was originally a prototype antenna for one of the most prominent telescopes of European Southern Observatory - ALMA - and Submillimeter Telescope (SMT). The CO(1→0) emission with a frequency of $\nu = 115.271$ GHz (2.6 mm) is approximately in the middle of the combined range of the telescopes covering routinely a window from 4.6 mm to 0.6 mm. However, the MASCOT survey is using the 12 m Telescope only.
The objectives stated by the MASCOT include [60]:

- Spatially-resolved scaling relations,

- link between the cold gas content and star formation,

- kinematics of the gas,

- interaction between the AGN and the interstellar medium.

Scaling relations of the CO content and parameters like stellar mass, star formation rate and the activity of the central AGN have been studied before using single-fibre spectroscopy. The spatial resolution provided by the IFU opens an opportunity to study various gradients across the galaxy, like the metallicity, the ionisation mechanism and the stellar age.
The second question is targeting the problem of the precise correlation between the star formation and the cold gas content. Thanks to the research done in the field during the past decades, the standard link is well understood. However, many galaxies (e.g. low-metallicity galaxies, starburst galaxies) show deviations from this relation. MASCOT can help shed light on this problem, studying some of the above stated parameters.
The kinematics of the gas of different phases is possible to study by comparing the MaNGA's detailed kinematics map of ionised gas with the integrated CO kinematics from ARO representing the molecular gas.
The last MASCOT goal, the link between the AGN activity and the ISM, is the subject of this thesis as explained in detail in Introduction.

# 5  Analysis of Properties of MASCOT Galaxies

In this chapter, a description of the analysis that was done to fulfil the goals stated in Introduction is provided. The chapter starts with a sample selection. MASCOT project combines data from two different surveys - MaNGA and ARO. The analysis of the MaNGA data is the subject of this work, therefore, it is rigorously described. On the other hand, the ARO part was done by the MASCOT collaboration and is presented in the next chapter. The section about the measurement of the size of the NLR of the MASCOT targets follows. The exact fitting procedure and assumptions that were made are presented.

## 5.1  Sample Selection

While the MaNGA survey has already targeted several thousands of galaxies the MASCOT, whose observations are also currently ongoing, less than a hundred. From the total of 83 (at the time of writing this thesis), the sub-sample of 11 targets flagged as a AGN-candidate by the MASCOT collaboration was selected. The process of detection of AGN-candidates can be found in works of Wylezalek [61], [62]. Their coordinates and redshifts are listed in the Table 5.1.

For each target, the flux map of [OIII] emission line derived from the DAP using the Python distribution of Marvin tool was created. On this map, a mask was applied, so that only spaxels flagged as AGN by the BPT diagnostics are taken into account. This was done for the SII-based and NII-based BPT diagrams separately as explained in Section 3.6.

Subsequently, the flux was converted to the surface brightness. The DAP provides the flux in the units of erg s$^{-1}$ cm$^{-2}$ spaxel$^{-1}$. Therefore, the conversion factor is 4 - the number of spaxels per arcsec$^2$ for the MaNGA survey.

The targets whose surface brightness maximum was under the threshold for the NLR definition stated in Section 3.6 were excluded from further analysis to remain consistent within this work. The excluded targets and their surface brightness maxima are listed in the Table 5.2.

Furthermore, the target 1-24423 was flagged as predominantly star forming without a significant number of AGN spaxels by the BPT diagnostics. Figure 7.1 in Appendix A shows the SDSS image of all four excluded targets. Figure 5.1 shows their BPT diagrams.

| MaNGA-ID | Plate-IFU | RA | DEC | z |
|----------|-----------|-----|-----|---|
| 12-193481 | 7443-12703 | 229.525575871 | 42.7458424664 | 0.0403 |
| 1-113712 | 7815-6104 | 319.193098655 | 11.0437407875 | 0.0807 |
| 1-278057 | 8257-9102 | 166.767438931 | 45.8221385038 | 0.0252 |
| 1-235576 | 8326-6102 | 215.017906947 | 47.1213302326 | 0.0704 |
| 1-620993 | 8341-12704 | 189.213252539 | 45.6511702678 | 0.0303 |
| 1-321739 | 8552-12701 | 226.431661417 | 44.4049023746 | 0.0283 |
| 1-90242 | 8553-1901 | 233.968342684 | 57.9026365222 | 0.0302 |
| 1-210736 | 8604-12702 | 246.654494422 | 39.1275427221 | 0.0353 |
| 1-24423 | 8626-12704 | 263.755218506 | 57.0524330139 | 0.0472 |
| 1-604907 | 8715-3702 | 119.920672417 | 50.8399725276 | 0.0544 |
| 1-316872 | 9042-12703 | 235.152678619 | 28.5124355207 | 0.0328 |

Tab. 5.1. The sample of galaxies used in the analysis. The MaNGA-ID is an unique identifier of every target within the MaNGA survey. The Plate-IFU corresponds to the specific observation of the given target. The same galaxy can be observed multiple times - in that case, the Plate-IFU changes and the MaNGA-ID remains the same. The RA, DEC and redshift of each target follow.

| MaNGA-ID | Plate-IFU | Max SB [erg s$^{-1}$ cm$^{-2}$ arcsec$^{-2}$] |
|----------|-----------|-----------------------------------------------|
| 1-278057 | 8257-9102 | $1.3 \times 10^{-17}$ |
| 1-210736 | 8604-12702 | $2 \times 10^{-17}$ |
| 1-278057 | 8257-9102 | $1.3 \times 10^{-17}$ |

Tab. 5.2. The targets excluded from the analysis because of the insufficient surface brightness. As can be seen in the column *Max SB*, the threshold $10^{-16}$ erg s$^{-1}$ cm$^{-2}$ arcsec$^{-2}$ is not reached by either of them.

35
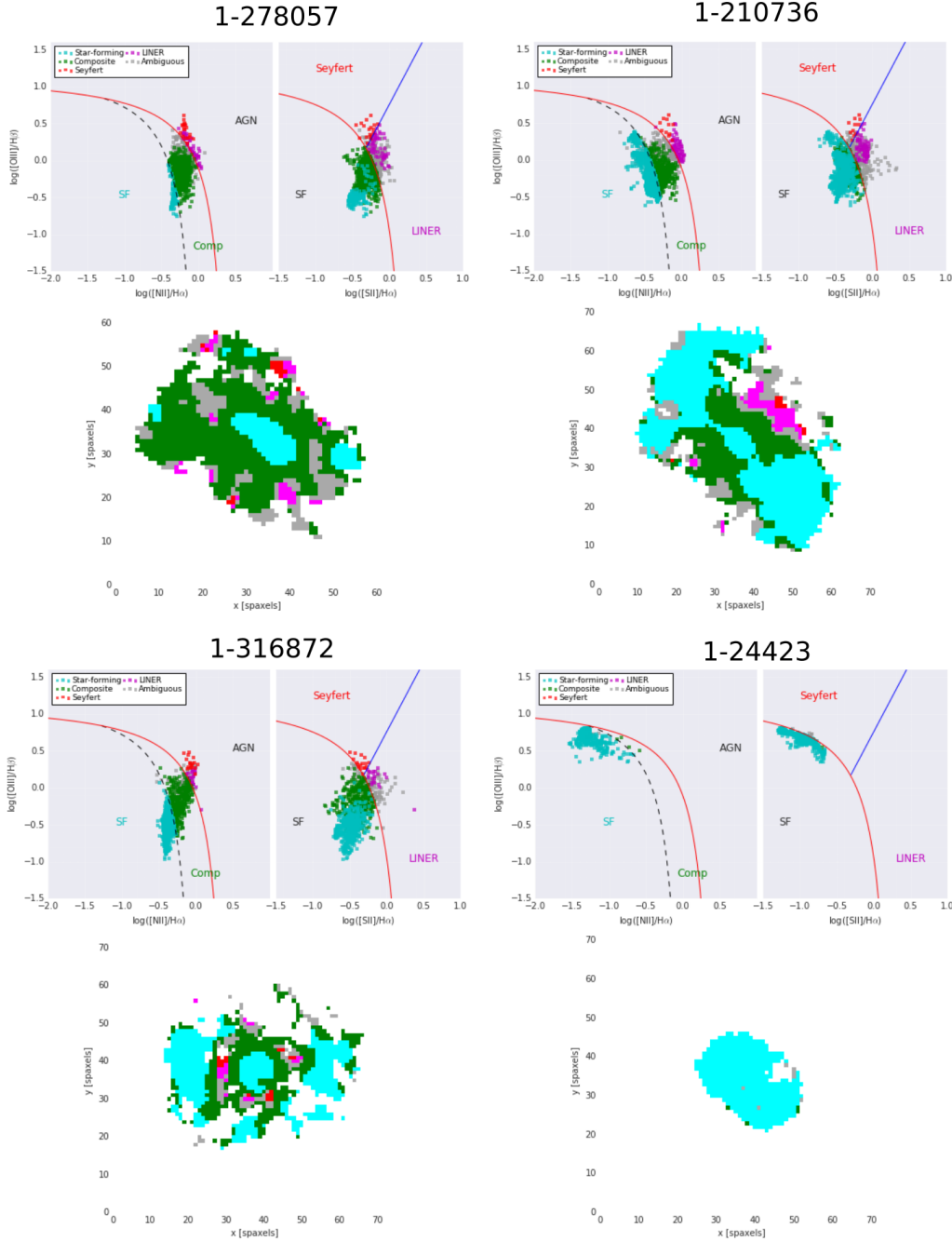
Fig. 5.1. BPT diagrams of the targets excluded from the analysis. The upper two gray plots of each image show the BPT diagnostic based on the NII and the SII emission line, respectively. As can be seen, the NII diagnostic can only distinguish between the star-formation induced ionization and the AGN induced ionization. The SII diagnostics also divides the targets according to their AGN type to LINERs and Seyferts, that differ in the strength of emission lines coming from the strongly ionized atoms. The bottom plot is the composite map of the spaxels. Each spaxel is flagged as AGN, star-forming or composite only if both SII and NII diagrams agree.

36

The rest of the targets were found suitable for the analysis for their sufficient surface brightness and the number of AGN-flagged spaxels. Their BPT diagrams can be found in the Appendix B of the thesis.

## 5.2 Size of the Narrow Line Region

The remaining 7 targets were further analysed. After the application of the mask allowing only the AGN-flagged spaxels to contribute, an appropriate way of the isophotes derivation was chosen. As explained before, the surface brightness isophote of a given value, $10^{-16}$ erg s$^{-1}$ cm$^{-2}$ arcsec$^{-2}$, is used for the definition of the size of the NLR. Therefore, a statistically significant number of isophotes based on the size of the target was fitted onto the [OIII] surface brightness map. The SDSS images of those 7 targets and their maps of [OIII] surface brightness after the application of the BPT-based mask are shown in Figures 5.2 and 5.3. The reason for their further division is explained below.

For the targets, whose map is regular and sufficiently bright, the Astropy Package for Photometry - *Photutils* - was used. In Photutils, the elliptical isophote analysis tool is already implemented in the *photutils.isophote* package. The isophotes in the image are set using an iterative method described by Jedrzejewski [63]. However, this package is only useful for elliptical targets. Irregular maps are not suitable for this algorithm. These targets were analysed using a tool of Matplotlib, Python 2D plotting library, called *contour* in the *axes* class [64]. This tool draws contours with defined values onto the 2D image. However, the provided information is much more difficult to process as demonstrated in Figure 5.4. Because the Matplotlib is a plotting tool, not a fitting tool, there is no way of extrapolation of the drawn isophotes on the whole map. Instead, the small unconnected areas remaining after the mask application are treated separately. For this reason, it is very challenging to draw conclusions about the whole map from this analysis.

As a first step, the targets analysed by the Photutils package were included in the survey. Figure 5.2 shows the targets analysed by Photutils package. Figure 5.3 shows the rest of the targets treated individually after plotting the isophotes onto their maps using the Matplotlib contour library.

### 5.2.1 Surface Brightness Radial Profile

The final goal of this part of analysis is to measure the size of the narrow-line region of each target. The definition used in this thesis is engaging the surface brightness isophote of given value. Intuitively, one could think that a simple elliptical fit onto the surface brightness map with the given value would be sufficient. However, this would lead to a large overestimation of the physical size of the NLR. Since the observation is strongly influenced by the effects of the atmosphere and instruments composing together a so-called *point spread function* (PSF), the true image of the target is "smeared" and the radial profile of the surface brightness appears wider. The effects of the PSF can be reduced when an analytical function describing the profile is found so that the observed curve can be
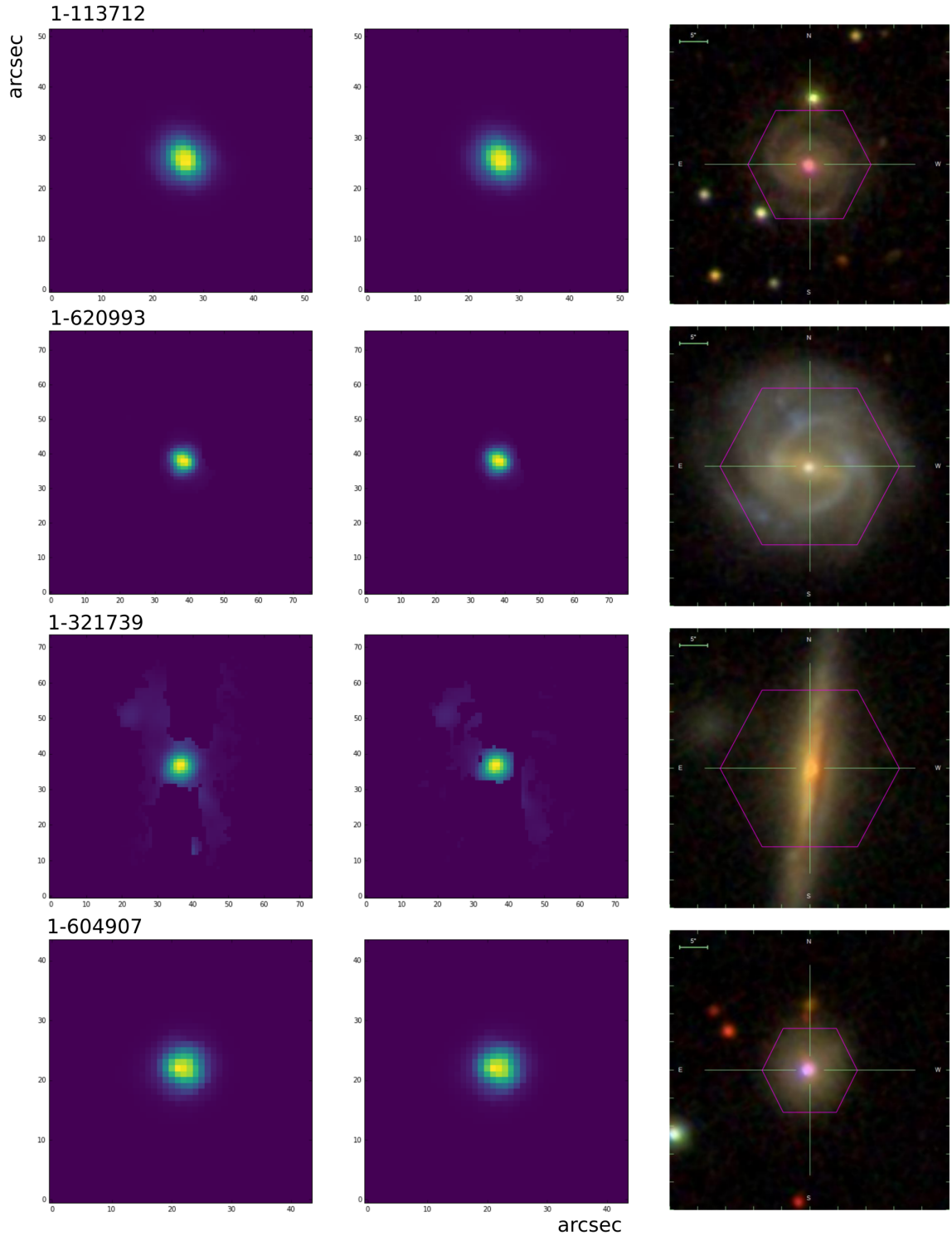
Fig. 5.2. Regular targets with sufficient surface brightness analysed by the Photutils package. The first two columns show maps of the [OIII] surface brightness after the application of the mask including AGN spaxels only. The masks are based on the SII and NII BPT diagnostics in this order. The third column shows the SDSS image of the galaxies.
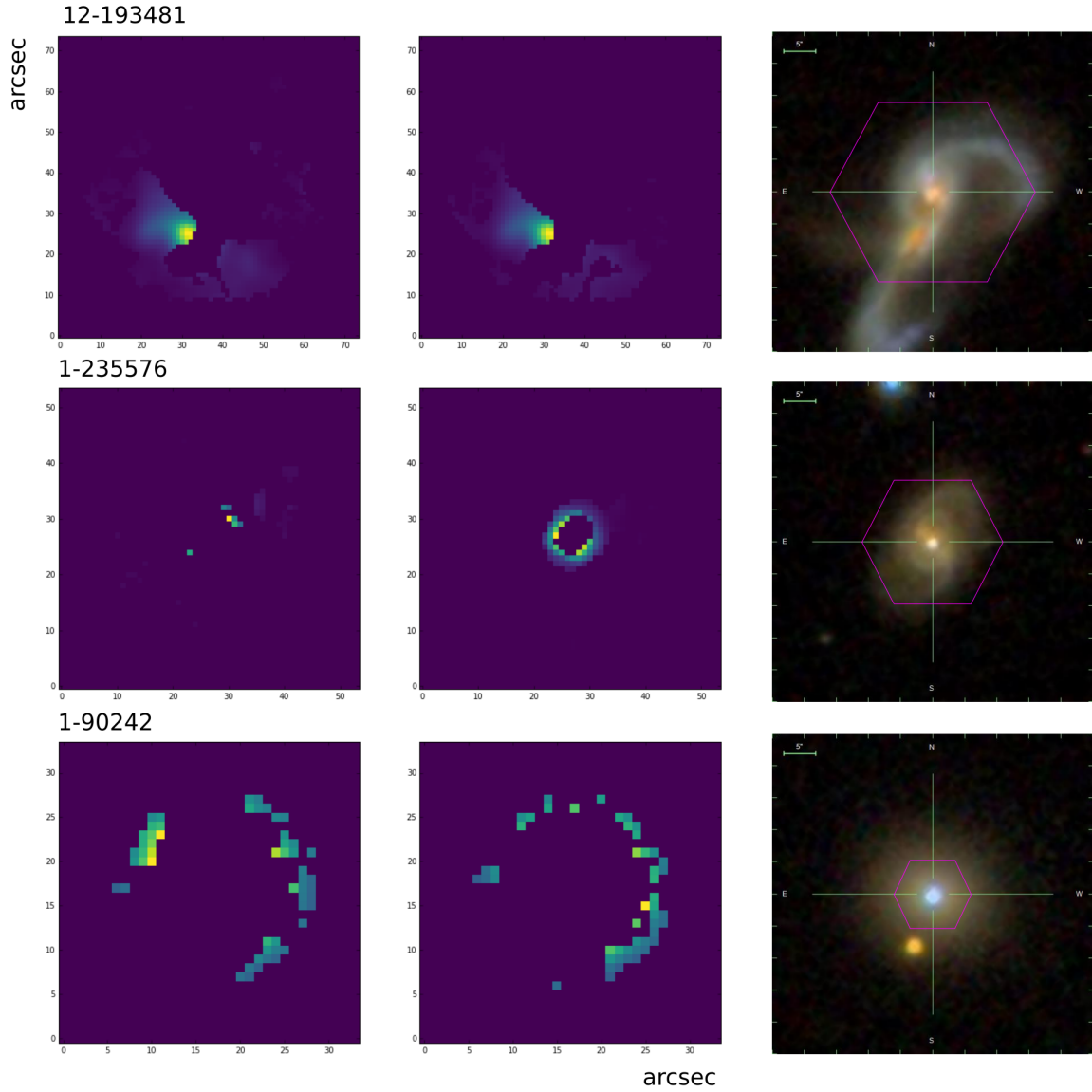
Fig. 5.3. Irregular targets with sufficient surface brightness analysed individually. The first two columns show maps of the [OIII] surface brightness after the application of the mask including AGN spaxels only. The masks are based on the SII and NII BPT diagnostics in this order. The third column again shows the SDSS image of the galaxies.

39
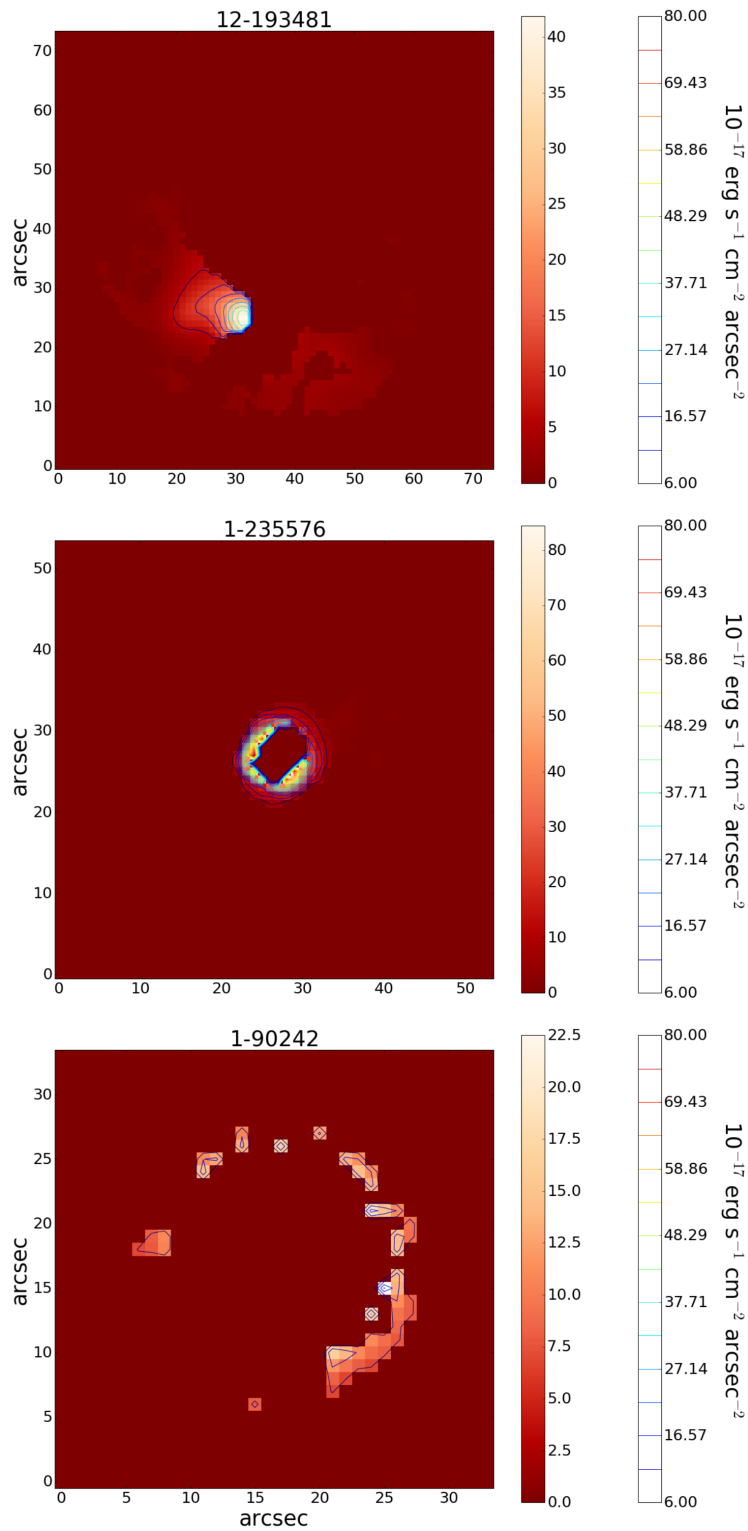
Fig. 5.4. Irregular targets with sufficient surface brightness analysed individually. Onto each map, contours corresponding to specific surface brightness value were drawn using the Matplotlib contour library. The first scale on the right shows the continuous range of the surface brightness of the whole map while the second discrete scale shows the brightness of the isophotes.

decomposed into this function and a Gaussian PSF, whose contribution is subsequently excluded from the analysis. The MaNGA experiment provides the user the exact parameters of the PSF in each band. The FWHM of the target-specific Gaussian PSF is one of the products of DRP. This presents an easy way of determination of the true size of the narrow-line region.

Firstly, the surface brightness map is fitted with a set of ellipses with a center in the pixel with the maximal intensity. From the resulting list of tens or even hundreds of isophotes (depending on the size of the target), a fixed number of isophotes is chosen to be fitted with an analytical function. The algorithm determines the number of isophotes to be extracted from the full list by estimating the physical size of the galaxy. Then, it divides them into three categories depending on the size. This is only an estimation because the apparent size of the galaxy is strongly influenced by the viewing angle. Therefore, this procedure is used just for consistency across the sample assuming that it will grow in size. As can be seen later, the number of isophotes - which is effectively the number of data points to be fitted in the next step - also determines the quality of the fit. Contra-intuitively, the increasing number of the data points does not necessarily lead to a better result. Therefore, for each target, three NLR measurements were done using a different number of the isophotes as is shown on the example of target 1-321739 in Figure 5.5. The rest of the figures can be found in Appendix C. Secondly, for each isophote, the mean distance from the galaxy center was calculated. At this point, for each target the set of several surface brightness values (corresponding to the individual isophotes) with their distances from the galaxy center was plotted as is shown on the example of target 1-113712 in Figure 5.6.

## ▉ 5.2.2 Radial profile de-convolution

For reason explained in the previous section, the resulting radial profile was fitted with a Gaussian PSF convolved with the *Sersic function* or *Sersic light distribution* describing how the intensity of galaxies changes with radius [65]

$$I(R) = I_e \exp\left\{-b_n \left[\left(\frac{R}{R_e}\right)^{1/n} - 1\right]\right\}, \tag{5.1}$$

where $R_e$ is half-light radius, $I_e$ is the intensity at $R_e$ and $n$ is the Sersic index controlling the curvature of the profile. With increasing Sersic index, steepness of the profile decreases. This means that galaxies with the lowest Sersic index have a large light concentration in their centres - typically disk galaxies with $n \approx 1$. Elliptical galaxies have $n \approx 4$ which corresponds to the *de Vaucouleurs profile*. The parameter $b_n$ is a function of this index and satisfies

$$\gamma(2n, b_n) = \frac{1}{2}\Gamma(2n). \tag{5.2}$$

The convolution was performed using two user-defined functions - Sersic and Gaussian using a library for least-squares minimization and data fitting in Python *LmFit*. This library allows the user to create a composite model of two previously defined models with arbitrary binary operator, in case of this work a convolution.
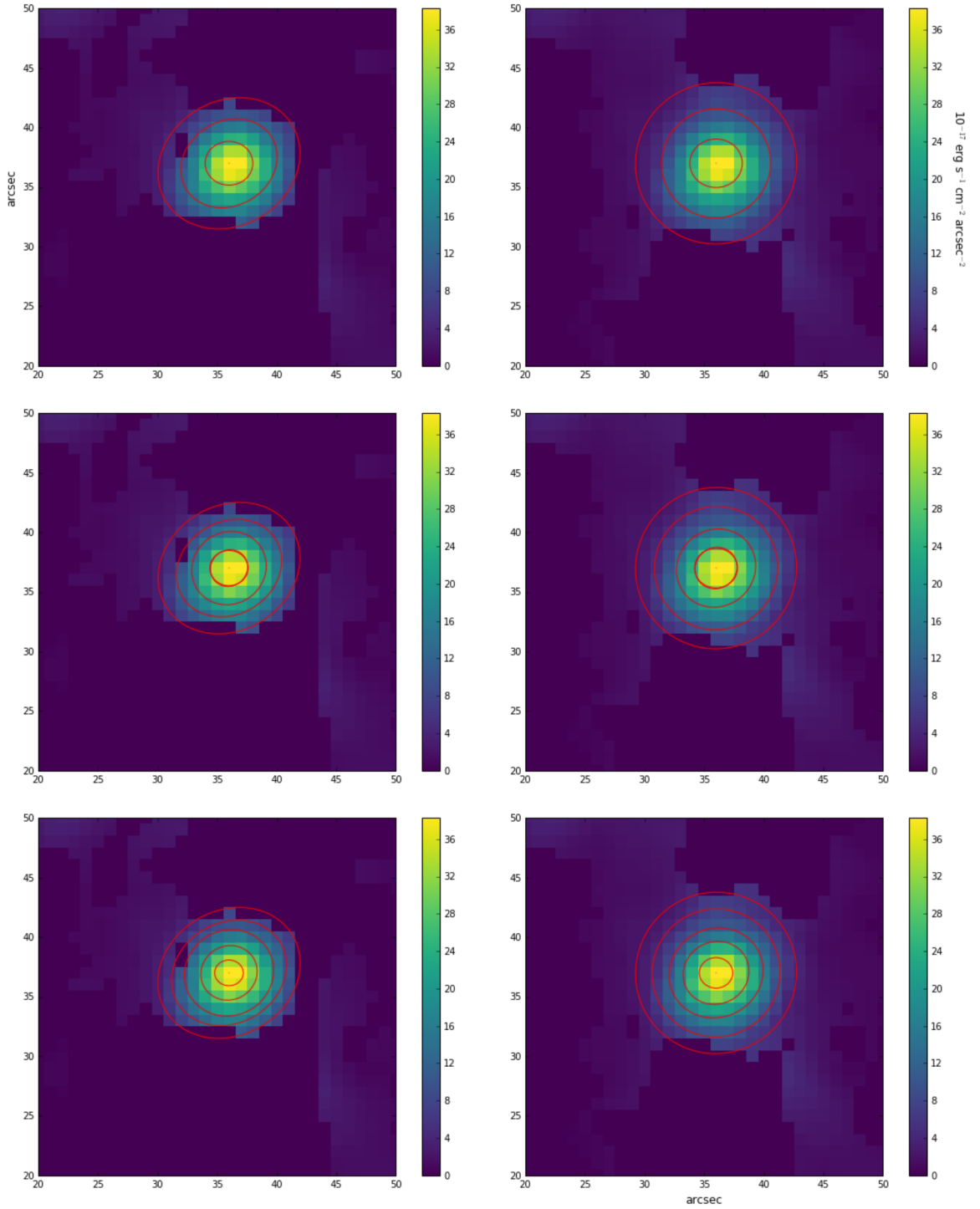
Fig. 5.5. Surface brightness isophotes fitted onto maps created using two different BPT diagnostics: the first column corresponds to the NII-emission-line-based map and the second column to the SII-emission-line-based map. A different number of isophotes was chosen for each of the targets depending on their size.
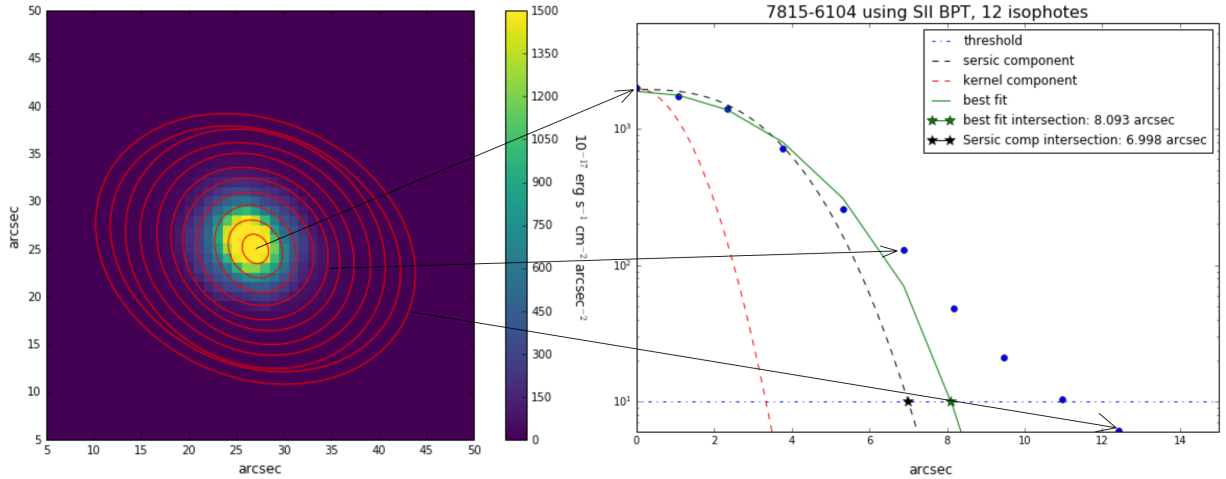
Fig. 5.6. Plot explaining the process of derivation of the radial profile. For a given number of surface brightness isophotes, the average distance from the brightest point was calculated. Each isophote represents one point in the right plot. The radial profile was subsequently fitted as described in Section 5.2.2.

First, the data was fitted with Sersic function only to get an estimate of starting parameters for the composite fit. Then, a fit using the convolved model was performed. The *LmFit* library allows to evaluate components of the composite model fit individually. To get the size of the narrow line region, the intersection of the Sersic component of the composite fit and a constant function corresponding to the chosen threshold value had to be found. The intersection was also found for the whole composite fit including the gaussian PSF to get a better idea of the caused overestimation.

As explained earlier, the number of isophotes corresponding to the number of data points in the fitted plot changes the quality of the fit. For this reason, each target was analysed using three different numbers of isophotes and two different BPT diagnostics (based on the NII and SII emission lines). In total, for each target 6 different sizes of the NLR were gained and can be found in Table 5.3. Analysis of one of the targets can be seen in Figure 7.9. The remaining targets can be found in the Appendix D.

To make sure that the final results are realistic, the sizes of narrow line region were plotted against the luminosity of the [OIII] emission line because this is a method used by other authors such as Chen [31] and Hainline [66]. Hainline used different threshold for the definition of NLR ($10^{-15}$ erg s$^{-1}$ cm$^{-2}$ arcsec$^{-2}$). This difference is marked as $R_{15}$ in case of Hainline and $R_{16}$ in case of Chen. In his work, Chen compares his result to the results of other IFU surveys. In this thesis, all three dependencies were compared with the gained results as can be seen in Figure 5.8.
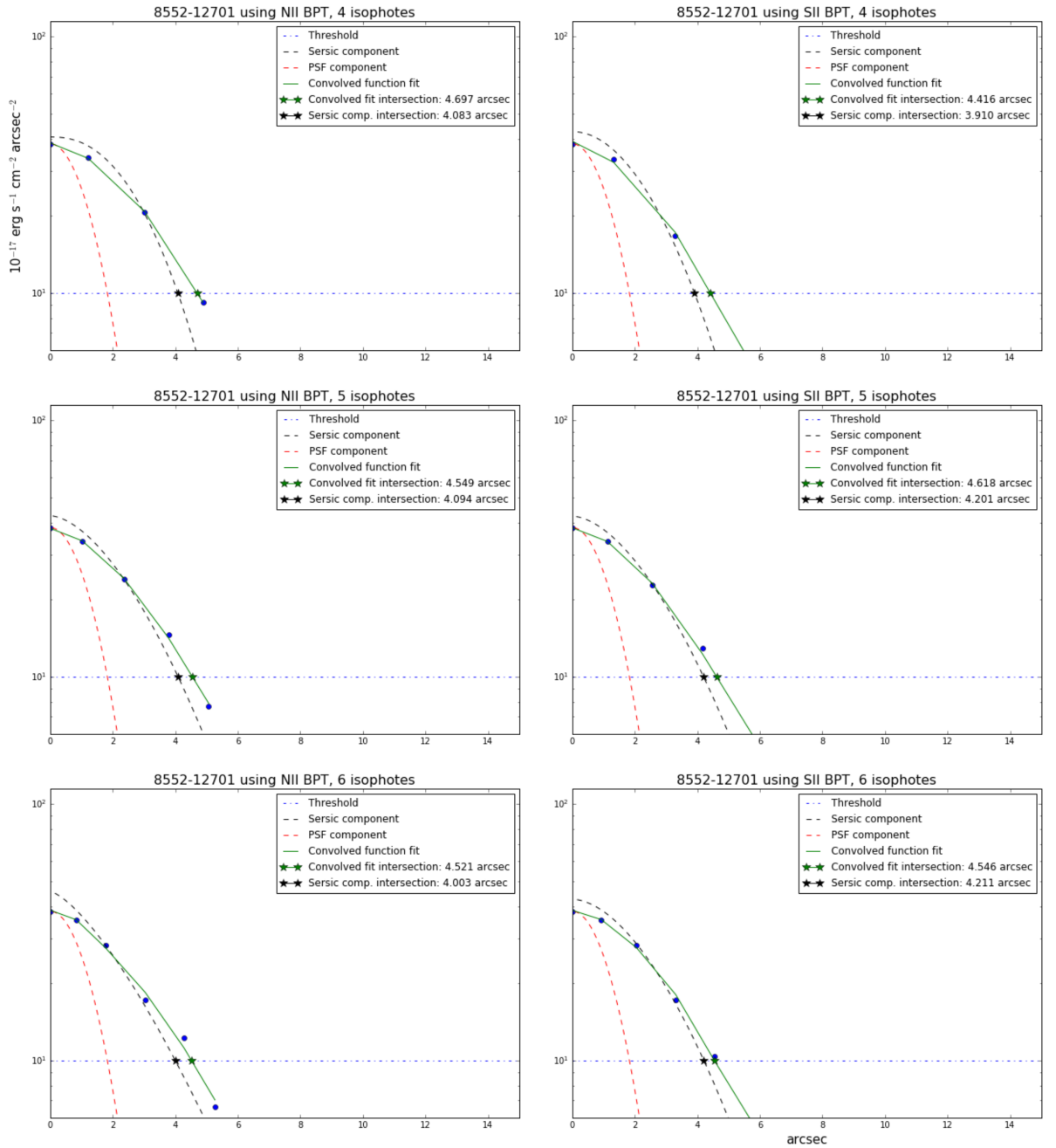
Fig. 5.7. Radial profiles of target 1-321739 derived from two different BPT diagnostics and three different numbers of isophotes. As can be seen, the fit quality changes with the number of isophotes as well as with the kind of BPT diagnostics. Using multiple options and their subsequent average leads to a reliable result. Plots show the fit using the convolved function, Sersic and PSF components, the threshold value and intersections with it.

| MaNGA-ID | # of isophotes | NII-fit | NII-Sersic | SII-fit | SII-Sersic [arcsec] |
|---|---|---|---|---|---|
| 1-113712 | 10 | 8.0 | 7.0 | 8.0 | 6.7 |
|  | 11 | 8.6 | 8.0 | 8.7 | 7.8 |
|  | 12 | 8.5 | 7.7 | 8.7 | 7.0 |
| 1-620993 | 6 | 5.5 | 3.5 | 5.5 | 3.6 |
|  | 7 | 5.5 | 3.7 | 5.5 | 3.8 |
|  | 8 | 5.4 | 3.6 | 5.8 | 4.6 |
| 1-321739 | 4 | 4.7 | 4.1 | 4.4 | 3.9 |
|  | 5 | 4.5 | 4.1 | 4.6 | 4.2 |
|  | 6 | 4.5 | 4.0 | 4.5 | 4.2 |
|  | 7 | - | - | 4.6 | 4.2 |
| 1-604907 | 10 | 7.8 | 6.3 | 7.8 | 6.3 |
|  | 11 | 7.7 | 6.3 | 7.7 | 6.3 |
|  | 12 | 7.3 | 5.4 | 7.3 | 5.4 |

Tab. 5.3. Sizes of the narrow line region of chosen galaxies derived as a cross-section of the fit using the convolved function with the threshold value (NII-fit and SII-fit) and the real sizes derived as a cross-section of the deconvolved function (Sersic profile) with the threshold function (NII-Sersic and SII-Sersic). The NII, SII respectively, corresponds to different BPT diagnostics used for the initial surface brightness analysis.
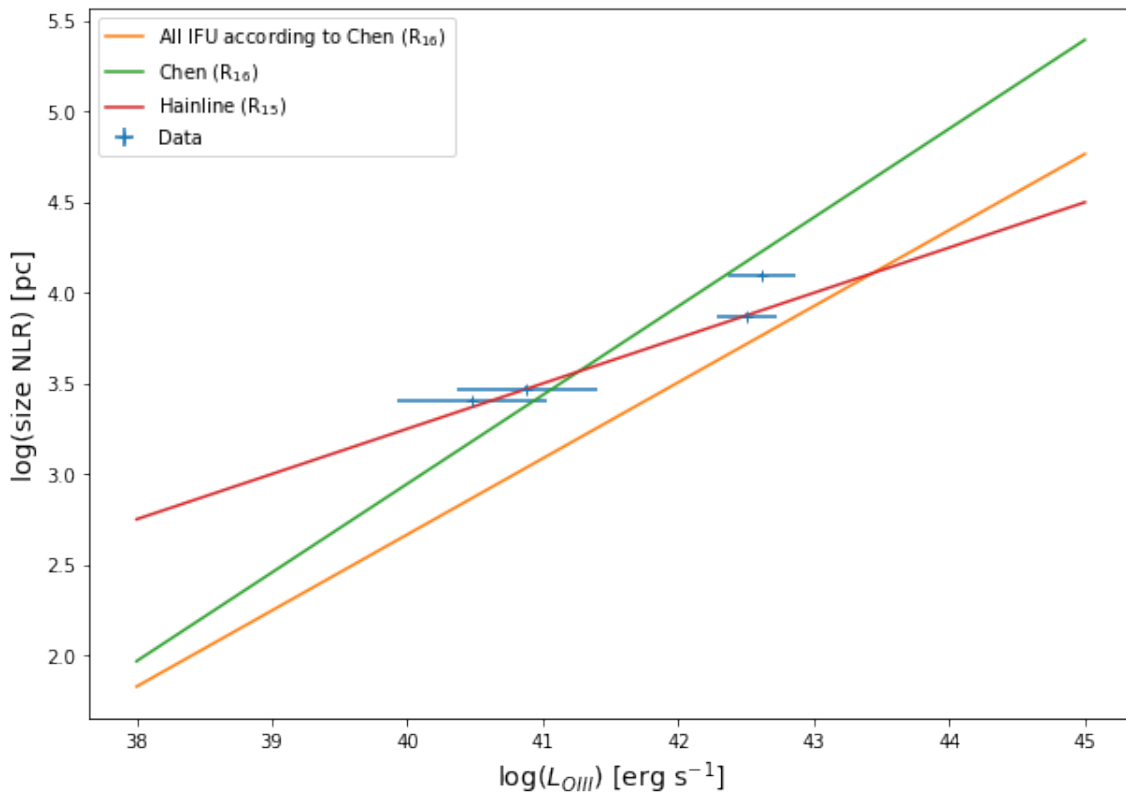


Fig. 5.8. Comparison of the results of this work with other IFU-based surveys, namely with Chen [31] and Hainline [66]. Generally, the data follow the previously observed dependence. For this reason, the results can be relied on.

# ■ 5.3 Cold Gas Content

With the knowledge of the size of NLR of MASCOT galaxies, it is finally possible to combine this information with the cold gas content in the given galaxy and reveal the potential correlation.

The cold gas content is traced using CO molecules that, unlike the more numerous $H_2$, have permanent dipole moment and are thus visible through their rotational spectrum. There is a non-trivial conversion between the observed CO luminosity and the mass of hydrogen molecules. However, for the purposes of this thesis, a demonstration of the basic relationship between cold gas content and the activity of the AGN is sufficient. Therefore, the conversion was not used and the size of NLR was connected directly to the CO flux from ARO. In case of two targets from the total of four, the requirement for a signal-to-noise ratio of 3 was not met. For this reason, instead of using the value of CO flux which is unreliable, the upper limit (UL) of its value was further analysed. The upper limit is given as three times the root mean square of the flux. Furthermore, it is convenient to normalize the cold gas content by the total stellar mass of the galaxy. As a consequence, the results from targets significantly different in size can be compared. The Table 5.4 shows the analysed targets, sizes of their NLR extracted in the previous chapter, their total CO flux (or its upper limit) and the stellar mass average (using both MASCOT and MaNGA values).

| MaNGA-ID | Size of NLR [kpc] | CO flux [erg s$^{-1}$ cm$^{-2}$] | M$_*$ [M$_\odot$] |
|----------|-------------------|----------------------------------|-------------------|
| 1-113712 | $12.4 \pm 0.4$ | $(3.8 \pm 1.3) \times 10^{-17}$ (UL) | $(3.14 \pm 0.04) \times 10^{10}$ |
| 1-620993 | $2.9 \pm 0.1$ | $(6.1 \pm 1.8) \times 10^{-17}$ | $(2.75 \pm 0.04) \times 10^{10}$ |
| 1-321739 | $2.56 \pm 0.01$ | $(6.1 \pm 1.2) \times 10^{-17}$ | $(2.34 \pm 0.02) \times 10^{10}$ |
| 1-604907 | $7.5 \pm 0.2$ | $(2.3 \pm 0.8) \times 10^{-17}$ (UL) | $(9.8 \pm 0.01) \times 10^{9}$ |

Tab. 5.4. Data combining MaNGA and ARO data under the MASCOT survey. For each target, the size of narrow line region derived from MaNGA data can be found. The next column shows the CO flux gained from ARO survey. For targets 1-113712 and 1-604907, upper limit of this quantity was used because of their insufficient signal-to-noise ratio. The last column shows the stellar mass of the target which was used for the normalization of the CO flux to get rid of the dependence on the size of the galaxy.

The resulting plot can be found in Figure 5.9. It shows the CO flux with respect to the size of narrow line region. With increasing size of the NLR, the CO flux significantly decreases. This could imply that a case of the negative feedback of the supermassive black hole on the cold gas content of its host galaxy was observed. The cold gas content subsequently influences the galaxy evolution because of its close relationship with star formation and other processes.
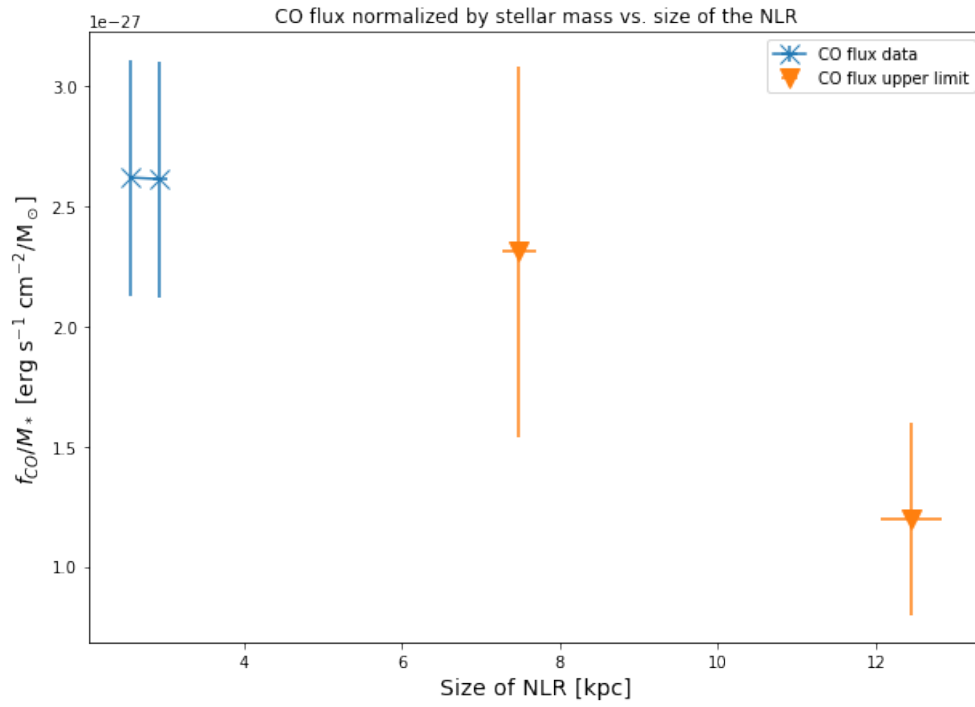
Fig. 5.9. The dependence of the CO flux on the size of the narrow line region. The uncertainty of the normalized flux is given as a combination of the uncertainties of the flux and the stellar mass. The uncertainty of the size of NLR is given as a standard deviation of average of the six values that were extracted for each target.

# 6 Results and Conclusions

The goal of this work was to study the influence of the active galactic nucleus on the properties of its host galaxy, namely on the cold gas content which is a prerequisite for the star formation. The assumption is such that with the increasing AGN activity, the cold gas content decreases due to multiple factors connected with it - among others outflows and strong radiation. Thanks to the multi-wavelength approach used in this thesis, different properties of target galaxies have been studied. Spatially resolved data of [OIII] surface brightness were provided by MaNGA, an extensive integral field spectroscopy survey. From the surface brightness analysis, the size of the narrow line region was derived which served as a proxy of the AGN activity. The second half of the information was provided by the ARO observatory in radio wavelengths. The $CO(1\rightarrow0)$ emission line was used as a tracer of molecular gas which is composed mostly of non-radiative $H_2$ molecules.

Before the analysis, an introduction of the necessary terms was given. Following the chapters dedicated to galaxies and active galactic nuclei, a chapter introducing the growing field of integral field spectroscopy and specific projects ensues. The analysis itself was performed in two phases - the measurement of the narrow line region of the targets and linking the results to the cold gas content information. The former was achieved by fitting the map of the [OIII] surface brightness with isophotes, followed by fitting the gained radial profile with Sersic function convolved with gaussian point spread function. After deconvolution, which removed the influence of the point spread function, the size of the narrow line region was found as an intersection of the bare Sersic function and a particular threshold which was chosen with an agreement with other works within the same field.

The main result of this work is the observed dependence of the molecular gas content of studied galaxies on the size of the narrow line region of the hosted AGN. It is clear that within the sample, with the increasing size of NLR, the molecular gas content tracked by the $CO(1\rightarrow0)$ emission line decreases. However, the sample is not very extensive and suffers from insufficient signal-to-noise ratio of some of the targets. Irregular targets, which cannot be analysed using the elliptical fitting procedure, were not involved in the final result derivation. As is stated in the Introduction, inclusion of these targets has been one of the goals of my contribution to this project. During the course of the thesis, a reliable algorithm for the analysis of irregular targets has not yet been devised due to the complex nature of the procedure. At minimum, an estimate could be

done based on the gained results, with the uncertainty of such values limiting the overall reliability of the analysis. Therefore, during the following stages of the project, this task will be given a priority. Furthermore, more targets will be included into the analysis as soon as they are observed as MASCOT project is still ongoing. With a large sample, a statistically significant conclusions can be drawn on what is at the moment only suggested with a limited sample.

The result of this work derived from a humble sample correlates with the results of other works. Therefore, it is probable that through multiple different mechanisms, AGN depletes the molecular gas in its host galaxy.

Kakkad et al. [67] studied an extensive sample of AGN-hosting galaxies and compared it to a sample of non-AGN galaxies with similar properties (e.g. star formation rate, redshift). Their results suggest a strong negative feedback of AGN - the depletion time (defined as a ratio of molecular gas mass and star formation rate) of studied non-AGN galaxies was found by the factor of 2 higher than that of AGN-hosting sample. Similarly, the luminosity of CO compared to the total infrared luminosity of studied galaxies is a factor of 2 higher for non-AGN galaxies. The paper does not conclude which mechanism in particular is responsible for this behaviour. However, it states that to study the influence of the AGN radiation on the molecular gas, the multi-wavelength approach needs to be employed as was done in this thesis.

In the paper by Fluetsch et al. [68], the molecular gas outflow is linked to the increasing AGN luminosity and with the black hole mass, which confirms that multiple mechanisms contribute to the negative feedback.

On the other hand, there are factors contributing to the complex picture of AGN-molecular gas content relationship that were not studied in this work. For example, an interesting result was achieved by Smolčić et al. [69] who studied AGNs of different accretion mechanisms - radiatively efficient and inefficient - and concluded that so-called *high excitation radio AGNs* have systematically higher molecular gas fraction. This result, in line with other works, suggests that high excitation radio AGNs are evolutionary younger thus have larger molecular gas reservoir to be transformed into stars.

In conclusion, the author believes that this work can serve as a starting point for the further investigation. However, there are several factors to be included before serious conclusions can be drawn. As can be seen from the short overview of papers concerning the subject under study, it is currently a topic of great interest in the community and with the boom of integral field spectroscopy and its interconnection with radio observatories, more data will be available for the deeper studies and understanding of the role of the AGNs in their host galaxies.

# Literature

[1] Ch. Harrison. Impact of supermassive black hole growth on star formation. *Nature Astronomy*, 1, 03 2017.

[2] L. Ferrarese and D. Merritt. A Fundamental Relation between Supermassive Black Holes and Their Host Galaxies. *The Astrophysical Journal*, 539(1):L9–L12, Aug 2000.

[3] K. Gebhardt and et al. Bender, R. A relationship between nuclear black hole mass and galaxy velocity dispersion. *The Astrophysical Journal*, 539(1):L13–L16, aug 2000.

[4] M. Gaspari and et al. Eckert, D. The x-ray halo scaling relations of supermassive black holes. *The Astrophysical Journal*, 884(2):169, oct 2019.

[5] J. Silk. Unleashing positive feedback: Linking the rates of star formation, supermassive black hole accretion, and outflows in distant galaxies. *The Astrophysical Journal*, 772(2):112, jul 2013.

[6] G. Cresci and R. Maiolino. Observing positive and negative agn feedback. *Nature Astronomy*, 2(3):179–180, Feb 2018.

[7] B. R. McNamara and et al. Russell, H. R. A mechanism for stimulating agn feedback by lifting gas in massive galaxies. *The Astrophysical Journal*, 830(2):79, oct 2016.

[8] G. Cresci and et al. Mainieri, V. Blowin' in the wind: Both negative and positive feedback in an obscured high-z quasar. *The Astrophysical Journal*, 799(1):82, jan 2015.

[9] L. S. Sparke and J. S. Gallagher. *Galaxies in the Universe: An Introduction.* Cambridge University Press, 2 edition, 2007.

[10] Cosmos The Swinburne Astronomy Online Encyclopedia. Cepheid variable stars. `https://astronomy.swin.edu.au/cosmos/C/cepheid+variable+stars`.

[11] M. A. Seeds and D. Backman. *Stars and Galaxies.* Cengage Learning, 2012.

[12] National Schools' Observatory. Galaxy classification. `https://www.schoolsobservatory.org/learn/astro/gals/class`.

[13] NASA. Multiwavelength milky way images. `https://asd.gsfc.nasa.gov/archive/mwmw/mmw_images.html`.

[14] H. Scheffler and H. Elsässer. *Physics of the Galaxy and Interstellar Matter.* Astronomy and astrophysics library. Springer-Verlag, 1987.

[15] J. Lequeux, E. Falgarone, and C. Ryter. *The Interstellar Medium.* Astronomy and Astrophysics Library. Springer Berlin Heidelberg, 2004.

[16] Space Telescope Scientific Institute. Star cluster ngc 602.

`https://hubblesite.org/image/3881`.

[17] B. M. Peterson. *An Introduction to Active Galactic Nuclei*. Cambridge University Press, 1997.

[18] F. Krauss, C. M. Urry, and P. Padovani. Unified Schemes for Radio-Loud Active Galactic Nuclei. *The Astronomical Journal*, 107:803, Sep 1995.

[19] M. A. Marshall and et al. Shabala, S. S. Triggering active galactic nuclei in galaxy clusters. *Monthly Notices of the Royal Astronomical Society*, 474(3):3615–3628, Nov 2017.

[20] D. J. Croton. Evolution in the Black Hole Mass–bulge Mass Relation: A Theoretical Perspective. *Monthly Notices of the Royal Astronomical Society*, 369(4):1808–1812, 07 2006.

[21] J. Magorrian and et al. Tremaine, S. The demography of massive dark objects in galaxy centers. *Astronomical Journal*, 115(6):2285–2305, jun 1998.

[22] J. Kormendy and L. C. Ho. Coevolution (or not) of supermassive black holes and host galaxies. *Annual Review of Astronomy and Astrophysics*, 51(1):511–653, 2013.

[23] R. Narayan and E. Quataert. Black hole accretion. *Science*, 307(5706):77–80, 2005.

[24] S. A. Balbus. Enhanced angular momentum transport in accretion disks. *Annual Review of Astronomy and Astrophysics*, 41(1):555–597, 2003.

[25] M. A. Abramowicz and P. Ch. Fragile. Foundations of black hole accretion disk theory. *Living Reviews in Relativity*, 16(1), Jan 2013.

[26] C. Miller. Accretion disks: Angular momentum. `https://www.astro.umd.edu/~miller/teaching/astr680/lecture10.pdf`.

[27] T. M. Heckman and P. N. Best. The coevolution of galaxies and supermassive black holes: Insights from surveys of the contemporary universe. *Annual Review of Astronomy and Astrophysics*, 52(1):589–660, 2014.

[28] T. M. Heckman and et al. Kauffmann G. Present-day growth of black holes and bulges: The sloan digital sky survey perspective. *The Astrophysical Journal*, 613(1):109–118, sep 2004.

[29] G. Kauffmann and T. M. Heckman. Feast and Famine: Regulation of Black Hole Growth in Low-redshift Galaxies. *Monthly Notices of the Royal Astronomical Society*, 397(1):135–147, 07 2009.

[30] G. Liu and et al. Zakamska, N. L. Observations of Feedback from Radio-quiet Quasars – I. Extents and Morphologies of Ionized Gas Nebulae. *Monthly Notices of the Royal Astronomical Society*, 430(3):2327–2345, 02 2013.

[31] J. Chen, Y. Shi, and et al. The spatial extension of extended narrow line regions in manga agn. *Monthly Notices of the Royal Astronomical Society*, 489(1):855–867, Aug 2019.

[32] J. A. Baldwin, M. M. Phillips, and R. Terlevich. Classification Parameters for the Emission-line Spectra of Extragalactic Objects. *Publications of the Astronomical Society of the Pacific*, 93:5–19, February 1981.

[33] L. J. Kewley and et al. Groves, B. The Host Galaxies and Classification of Active Galactic Nuclei. *Monthly Notices of the Royal Astronomical Society*, 372(3):961–976, November 2006.

[34] ESO. Integral field units.
https://www.eso.org/public/teles-instr/technology/ifu/.

[35] K. Bundy and et al. Bershady, M. A. Overview of the SDSS-IV MaNGA Survey: Mapping nearby Galaxies at Apache Point Observatory. *The Astrophysical Journal*, 798(1):7, Jan 2015.

[36] J. Allington-Smith. Basic principles of integral field spectroscopy. *New Astronomy Reviews*, 50(4):244 – 251, 2006. Integral Field Spectroscopy: Techniques and Data Production.

[37] D. Ren and J. Allington-Smith. On the application of integral field unit design theory for imaging spectroscopy. *Publications of the Astronomical Society of the Pacific*, 114(798):866–878, aug 2002.

[38] J. Allington-Smith and R. Content. Sampling and background subtraction in fiber-lenslet integral field spectrographs. *Publications of the Astronomical Society of the Pacific*, 110(752):1216–1234, oct 1998.

[39] R. Bacon and G. Monnet. *Data Analysis*. John Wiley and Sons, Ltd, 2017.

[40] J. M. Hill. The history of multiobject fiber spectroscopy. In S. C. Barden, editor, *Fiber Optics in Astronomy*, volume 3 of *Astronomical Society of the Pacific Conference Series*, page 77, January 1988.

[41] M. Cappellari and et al. Emsellem, E. The ATLAS3D project – VII. A New Look at the Morphology of nearby Galaxies: The Kinematic Morphology–density Relation. *Monthly Notices of the Royal Astronomical Society*, 416(3):1680–1696, 09 2011.

[42] M. A. Bershady and et al. Verheijen, M. A. W. The diskmass survey. i. overview. *The Astrophysical Journal*, 716(1):198–233, May 2010.

[43] P. D. Sackett. Does the milky way have a maximal disk? *The Astrophysical Journal*, 483(1):103–110, Jul 1997.

[44] S. W. Campbell and et al. D'Orazi, V. Sodium content as a predictor of the advanced evolution of globular cluster stars. *Nature*, 498(7453):198–200, May 2013.

[45] N. R. Tanvir and et al. Levan, A. J. The emergence of a lanthanide-rich kilonova following the merger of two neutron stars. *The Astrophysical Journal*, 848(2):L27, Oct 2017.

[46] R. Genzel and et al. Schreiber, N. M. Strongly baryon-dominated disk galaxies at the peak of galaxy formation ten billion years ago. *Nature*, 543(7645):397–401, Mar 2017.

[47] R. Bacon and et al. Conseil, S. The muse hubble ultra deep field survey - i. survey description, data reduction, and source detection. *A&A*, 608:A1, 2017.

[48] J. E. Gunn, W. A. Siegmund, and et al. Mannery, E. J. The 2.5 m telescope of the sloan digital sky survey. *The Astronomical Journal*, 131(4):2332–2359, Apr 2006.

[49] N. Drory and et al. MacDonald, N. The MaNGA Integral Field Unit Fiber Feed System for the Sloan 2.5 m Telescope. *The Astrophysical Journal*, 149(2):77, Feb 2015.

[50] S. A. Smee and et al. Gunn, J. E. The multi-object, fiber-fed spectrographs for the sloan digital sky survey and the baryon oscillation spectroscopic

survey. *The Astronomical Journal*, 146(2):32, Jul 2013.

[51] D. R. Law and et al. Yan, R. Observing strategy for the sdss-iv/manga ifu galaxy survey. *The Astronomical Journal*, 150(1):19, jun 2015.

[52] B. Husemann and S. F. et al. Sánchez. The califa survey: Calibration plan. In *The Science of Calibration*, volume 503 of *Astronomical Society of the Pacific Conference Series*, page 111, May 2016.

[53] B. L. Lee. Ccd theory. https://users.astro.ufl.edu/~lee/ast325/handouts/ccd.pdf.

[54] D. R. Law and et al. Cherinka, B. The data reduction pipeline for the sdss-iv manga ifu galaxy survey. *The Astronomical Journal*, 152(4):83, Sep 2016.

[55] B. Cherinka and B. H. et al. Andrews. Marvin: A tool kit for streamlined access and visualization of the sdss-iv manga data set. *The Astronomical Journal*, 158(2):74, Jul 2019.

[56] K. B. Westfall and et al. Cappellari, M. The data analysis pipeline for the sdss-iv manga ifu galaxy survey: Overview. *The Astronomical Journal*, 158(6):231, Nov 2019.

[57] M. S. Bessell. Standard photometric systems. *Annual Review of Astronomy and Astrophysics*, 43(1):293–336, 2005.

[58] B. Abolfathi and et al. Charles, C. Kirkpatrick IV. The fourteenth data release of the sloan digital sky survey: First spectroscopic data from the extended baryon oscillation spectroscopic survey and from the second phase of the apache point observatory galactic evolution experiment. *Astrophysical Journal Supplement Series*, 235, 4 2018.

[59] D. Aguado and et al. Prakash, A. The fifteenth data release of the sloan digital sky surveys: First release of manga-derived quantities, data visualization tools, and stellar library. *Astrophysical Journal Supplement Series*, 240, 02 2019.

[60] D. Wylezalek. About the mascot program. http://www.eso.org/~dwylezal/mascot.

[61] D. Wylezalek and et al. Zakamska, N. L. Sdss-iv manga: Identification of active galactic nuclei in optical integral field unit surveys. *Monthly Notices of the Royal Astronomical Society*, 474(2):1499–1514, February 2018.

[62] D. Wylezalek and et al. Flores, A. M. Ionized gas outflow signatures in sdss-iv manga active galactic nuclei. *Monthly Notices of the Royal Astronomical Society*, 492(4):4680–4696, March 2020.

[63] R. I. Jedrzejewski. CCD Surface Photometry of Elliptical Galaxies - I. Observations, Reduction and Results. *Monthly Notices of the Royal Astronomical Society*, 226:747–768, June 1987.

[64] Matplotlib development team. Matplotlib documentation. https://matplotlib.org/api/_as_gen/matplotlib.axes.Axes.contour.html.

[65] I. Trujillo, A. W. Graham, and N. Caon. On the Estimation of Galaxy Structural Parameters: the Sérsic model. *The Astrophysical Journal*, 326(3):869–876, September 2001.

[66] K. N. Hainline and et al. Hickox, R. Salt long-slit spectroscopy of luminous obscured quasars: An upper limit on the size of the narrow-line region? *The*

*Astrophysical Journal*, 774(2):145, Aug 2013.

[67] D. Kakkad and et al. Mainieri, V. Alma observations of cold molecular gas in agn hosts at z ∼ 1.5 – evidence of agn feedback? *Monthly Notices of the Royal Astronomical Society*, 468(4):4205–4215, Apr 2017.

[68] A. Fluetsch and et al. Maiolino, R. Cold molecular outflows in the local Universe and their feedback effect on galaxies. *Monthly Notices of the Royal Astronomical Society*, 483(4):4586–4614, 12 2018.

[69] V. Smolčić and D. A. Riechers. The molecular gas content of z < 0.1 radio galaxies: Linking the active galactic nucleus accretion mode to host galaxy properties. *The Astrophysical Journal*, 730(2):64, Mar 2011.

# List of figures

# List of tables

# 7 Appendix

## Appendix A



Fig. 7.1. The targets excluded from the analysis due to their insufficient surface brightness. The purple hexagon shows the extent of a fibre bundle. The last target, 1-24423, is flagged as star forming by the BPT, therefore unsuitable for further analysis.
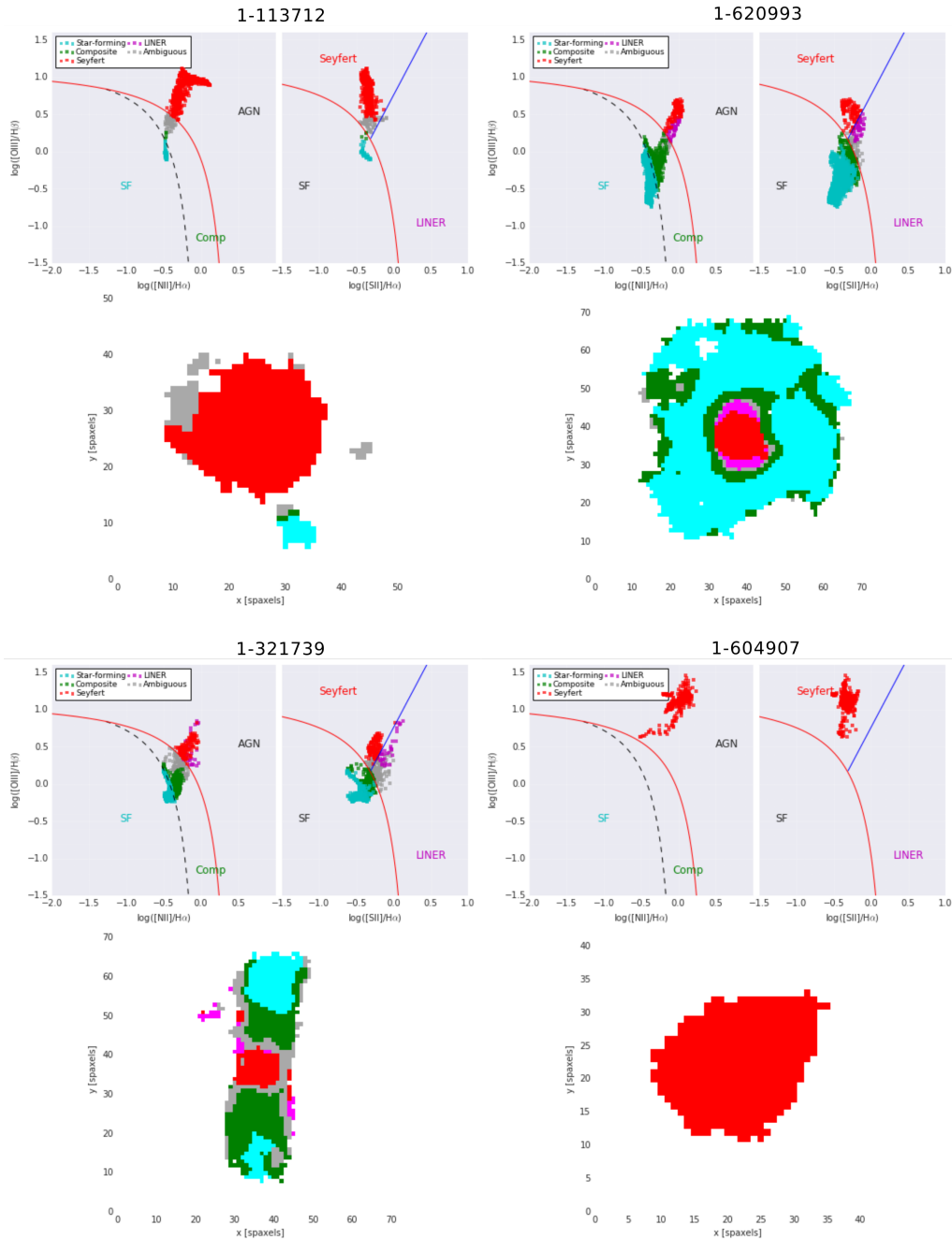
# Appendix B



Fig. 7.2. BPT diagrams of the targets included to the analysis. The upper two gray plots of each image show the BPT diagnostic based on NII emission line, SII respectively. As can be seen, the NII diagnostic can only distinguish between the star-formation induced ionization and the AGN induced ionization. The SII diagnostics also divides the targets according to their AGN type to LINERs and Seyferts that differ in the strength of emission lines coming from the strongly ionized atoms. The bottom plot is the composite map of the spaxels. Each spaxel is flagged as AGN, star-forming or composite only if both SII and NII diagrams agree.
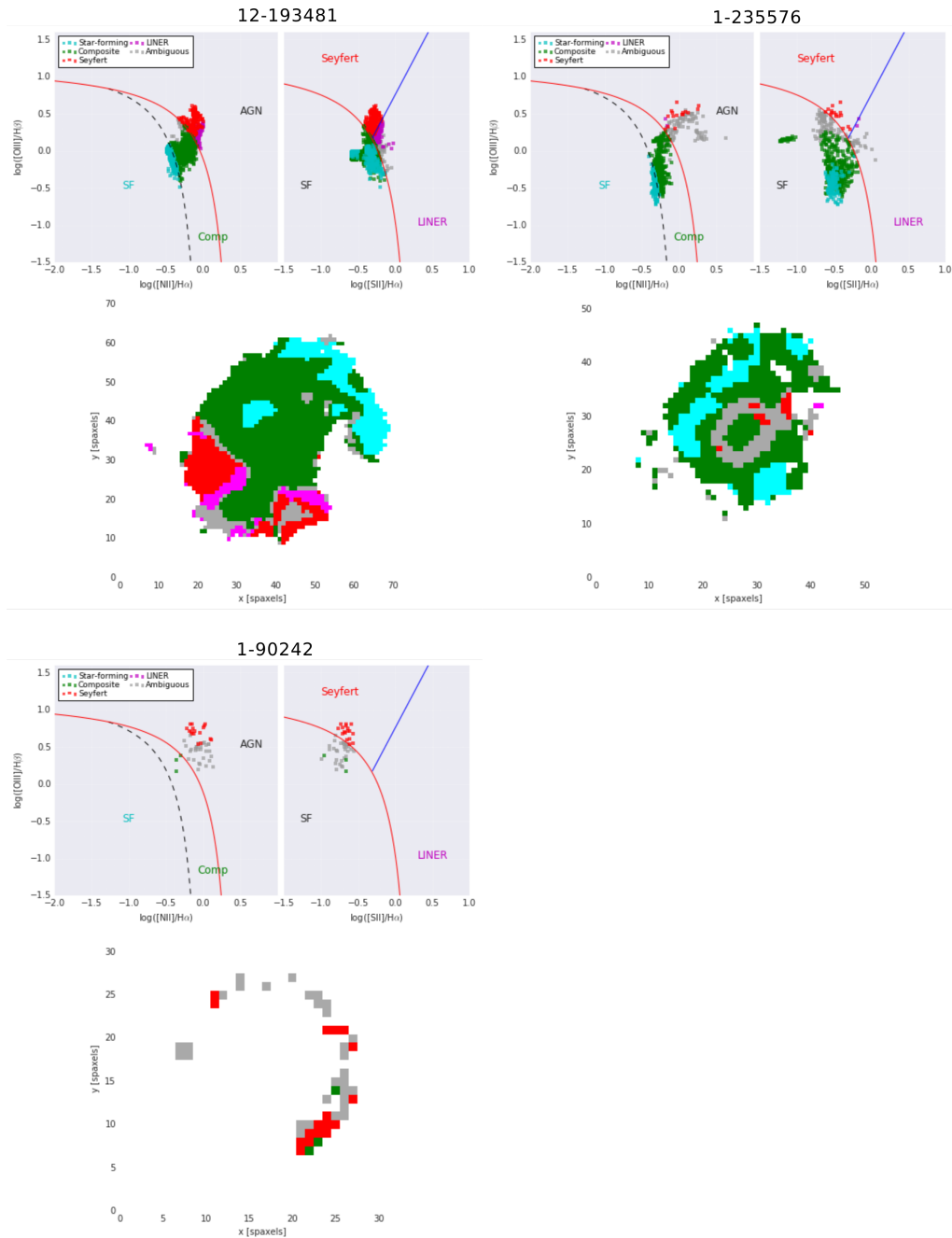
Fig. 7.3. BPT diagrams of irregular targets that cannot be analysed using the standard procedure using elliptical isophotes fitting. The description of the figures is the same as in the previous case.
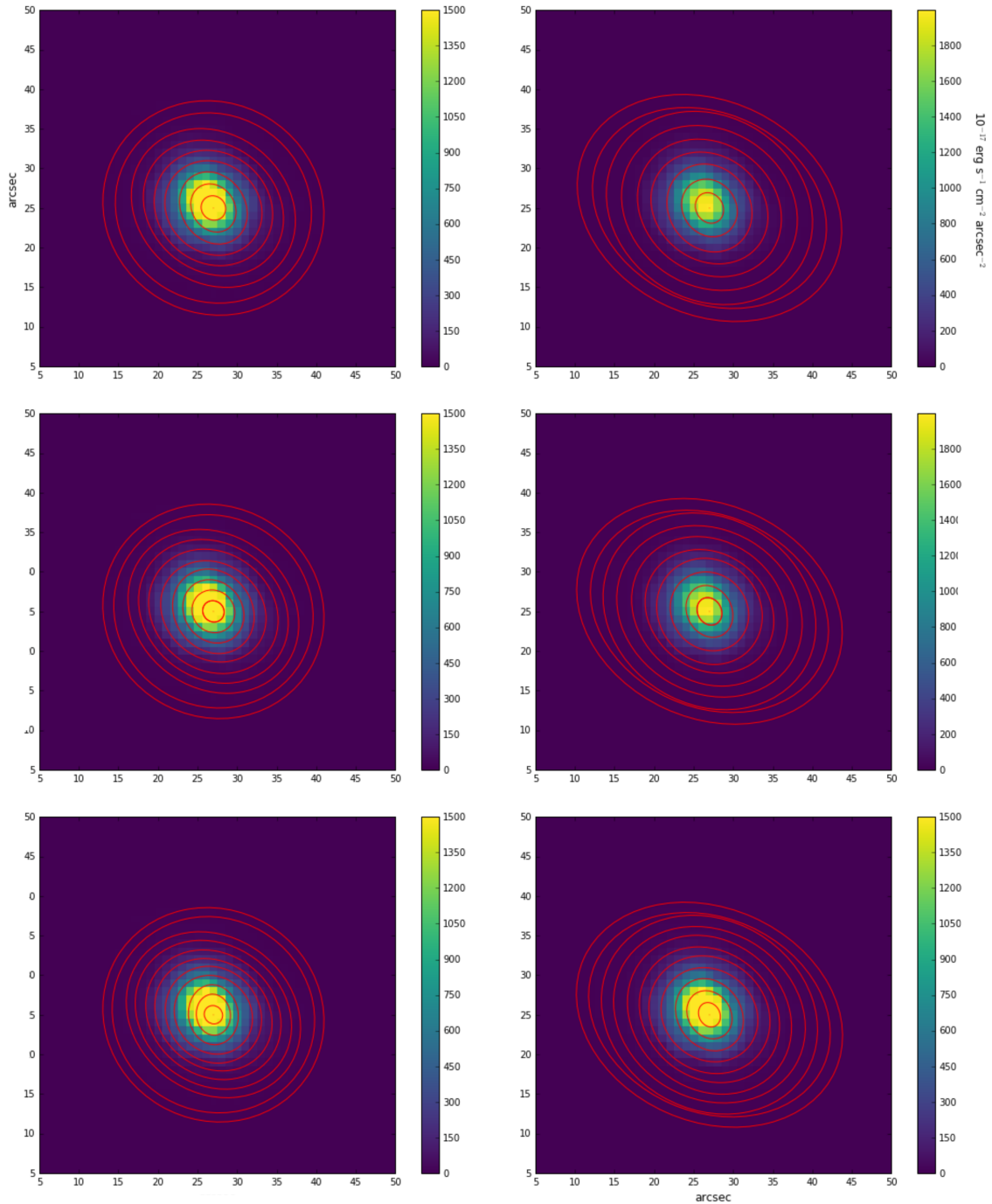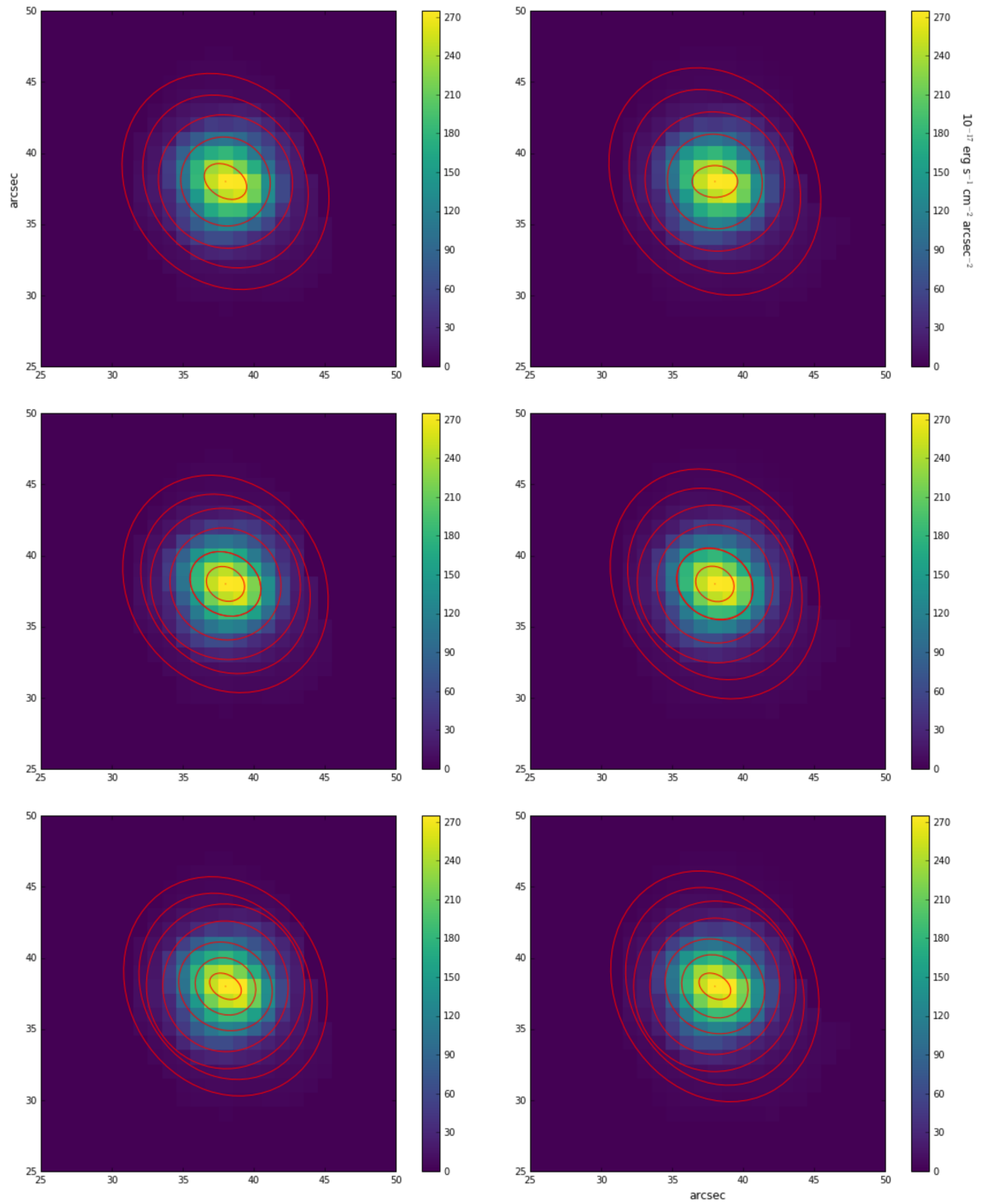
# Appendix C



Fig. 7.4. Surface brightness isophotes fitted onto maps of target 1-113712 created using two different BPT diagnostics: the first column corresponds to the NII-emission-line-based map and the second column to the SII-emission-line-based map. For this target, 10, 11 and 12 isophotes were fitted.
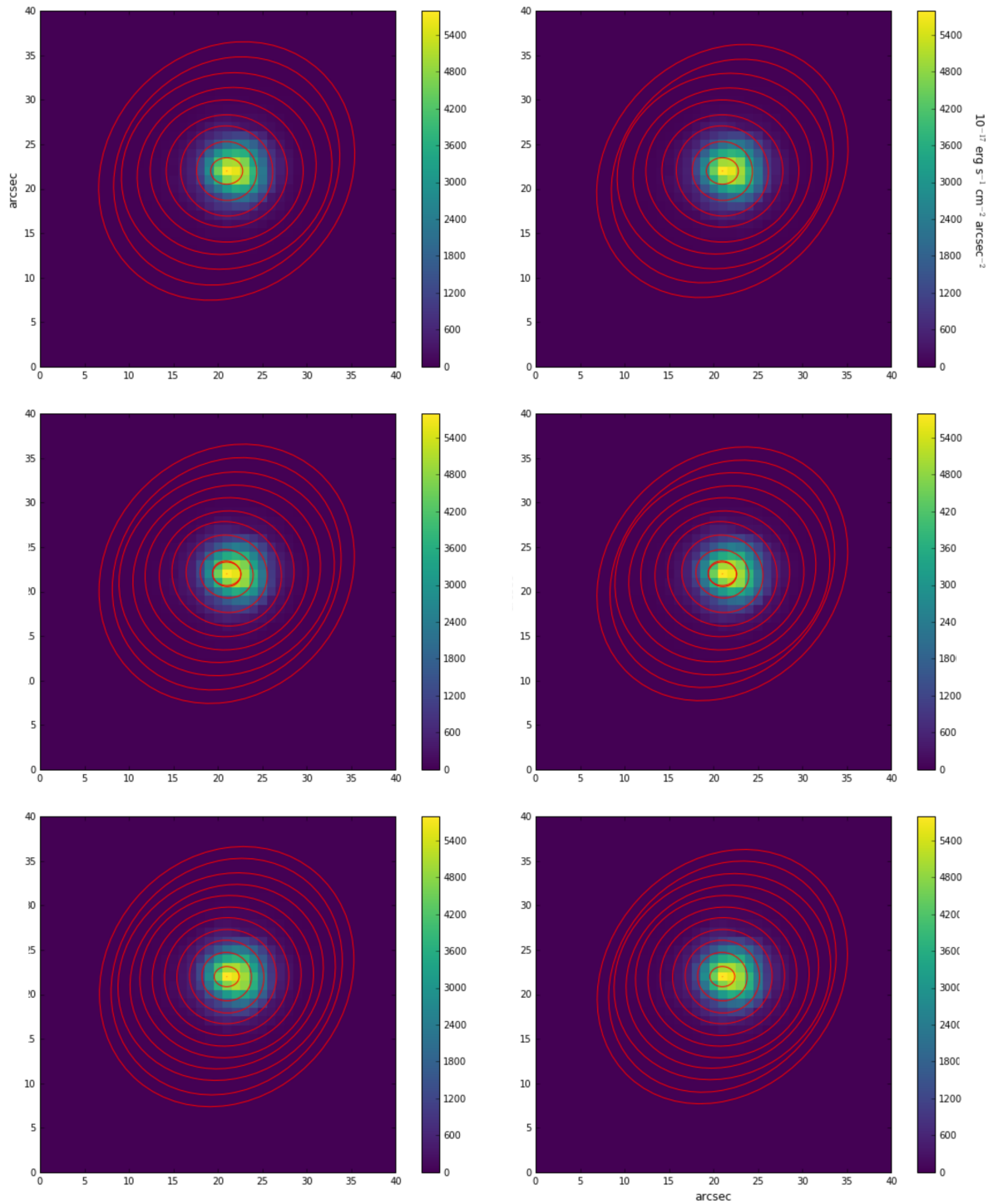
Fig. 7.5. Surface brightness isophotes fitted onto maps of target 1-620993 created using two different BPT diagnostics: the first column corresponds to the NII-emission-line-based map and the second column to the SII-emission-line-based map. For this target, 6, 7 and 8 isophotes were fitted.

Fig. 7.6. Surface brightness isophotes fitted onto maps of target 1-604907 created using two different BPT diagnostics: the first column corresponds to the NII-emission-line-based map and the second column to the SII-emission-line-based map. For this target, 10, 11 and 12 isophotes were fitted.
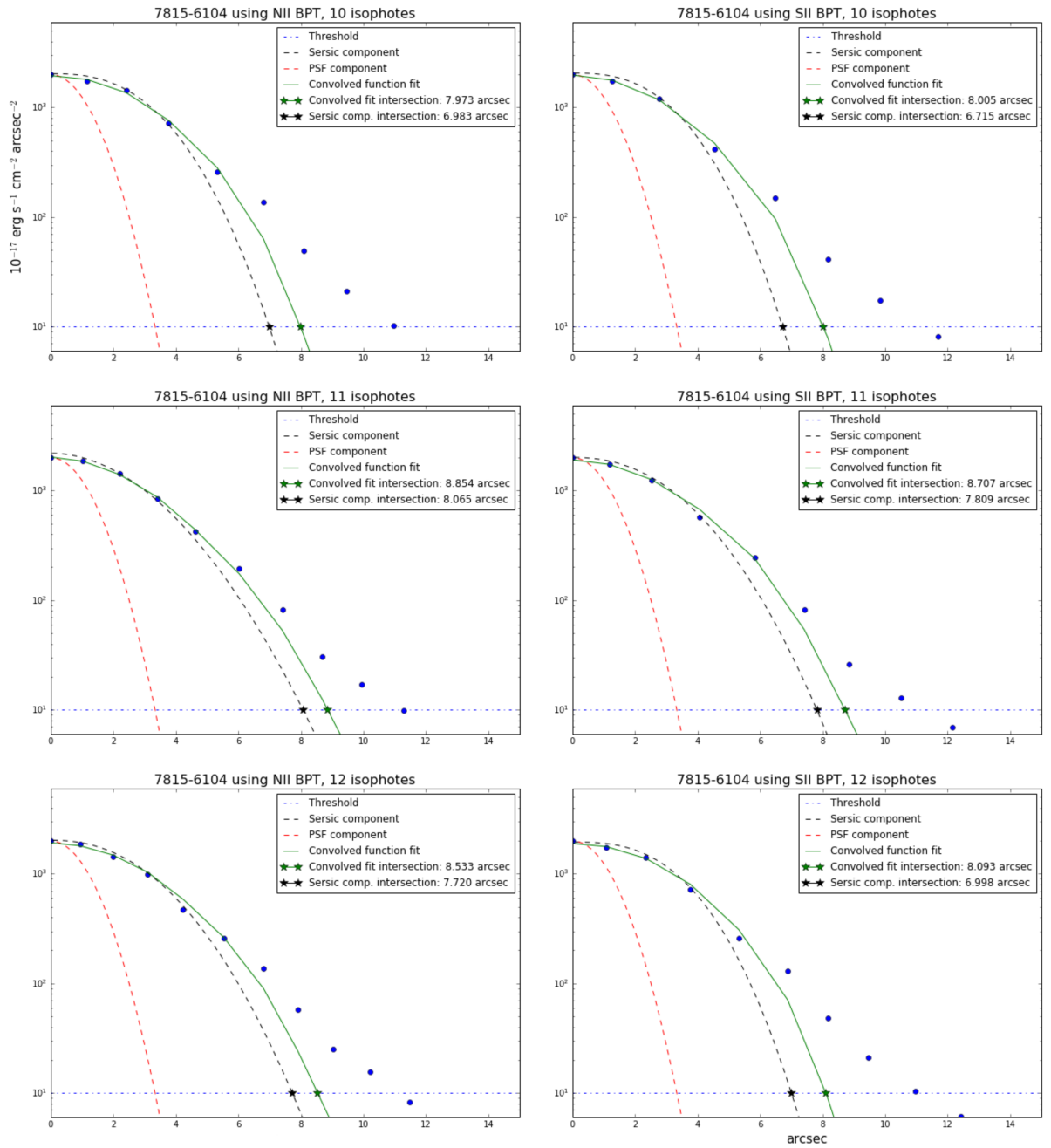
# Appendix D



Fig. 7.7. Radial profiles of target 1-113712 derived from two different BPT diagnostics and three different numbers of isophotes. As can be seen, the fit quality changes with the number of isophotes as well as with the kind of BPT diagnostics. Using multiple options and their subsequent average leads to the reliable result. Plots show the fit using the convolved function, Sersic and PSF components, the threshold value and intersections with it.
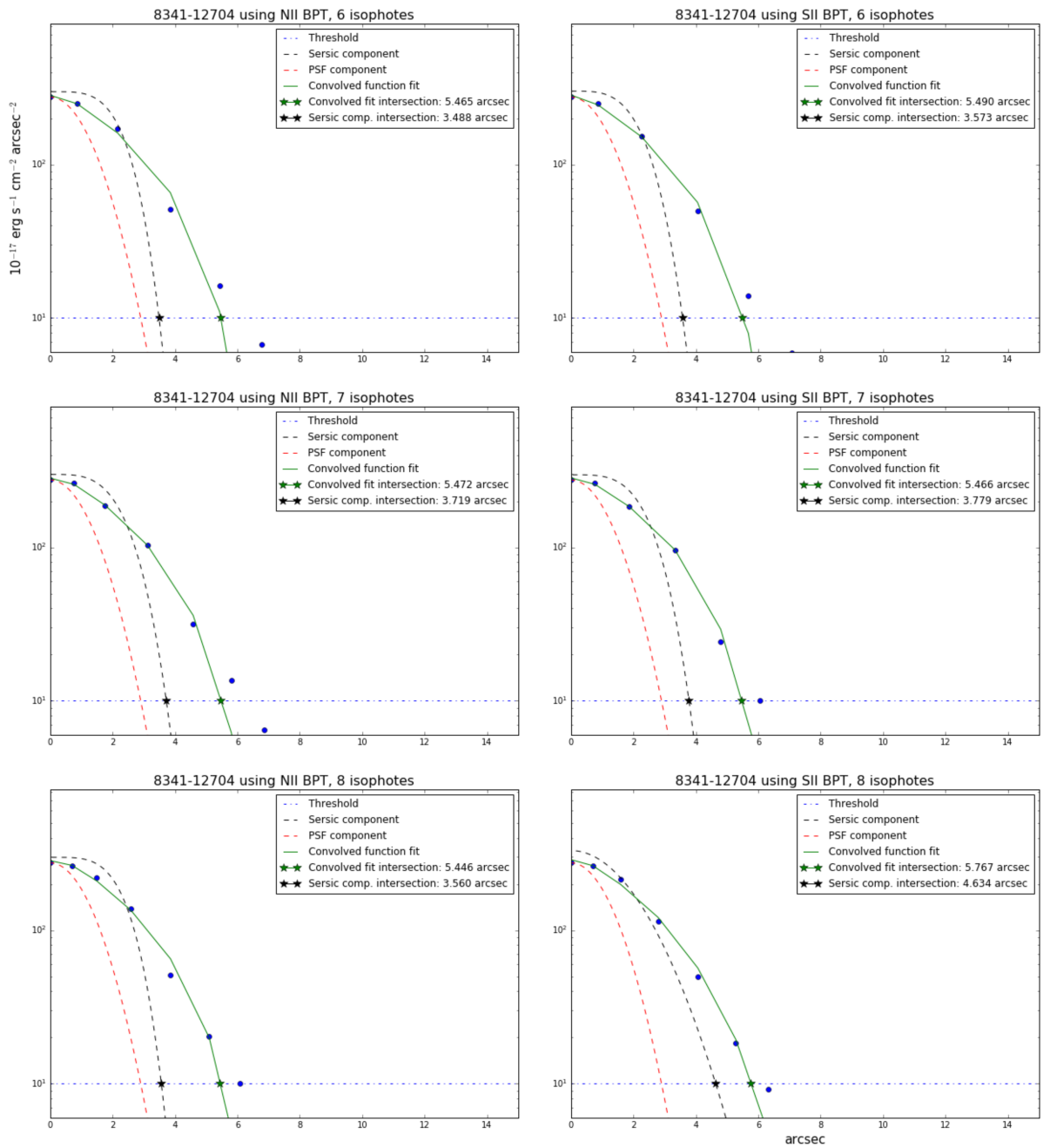
Fig. 7.8. Radial profiles of target 1-620993 derived from two different BPT diagnostics and three different numbers of isophotes.
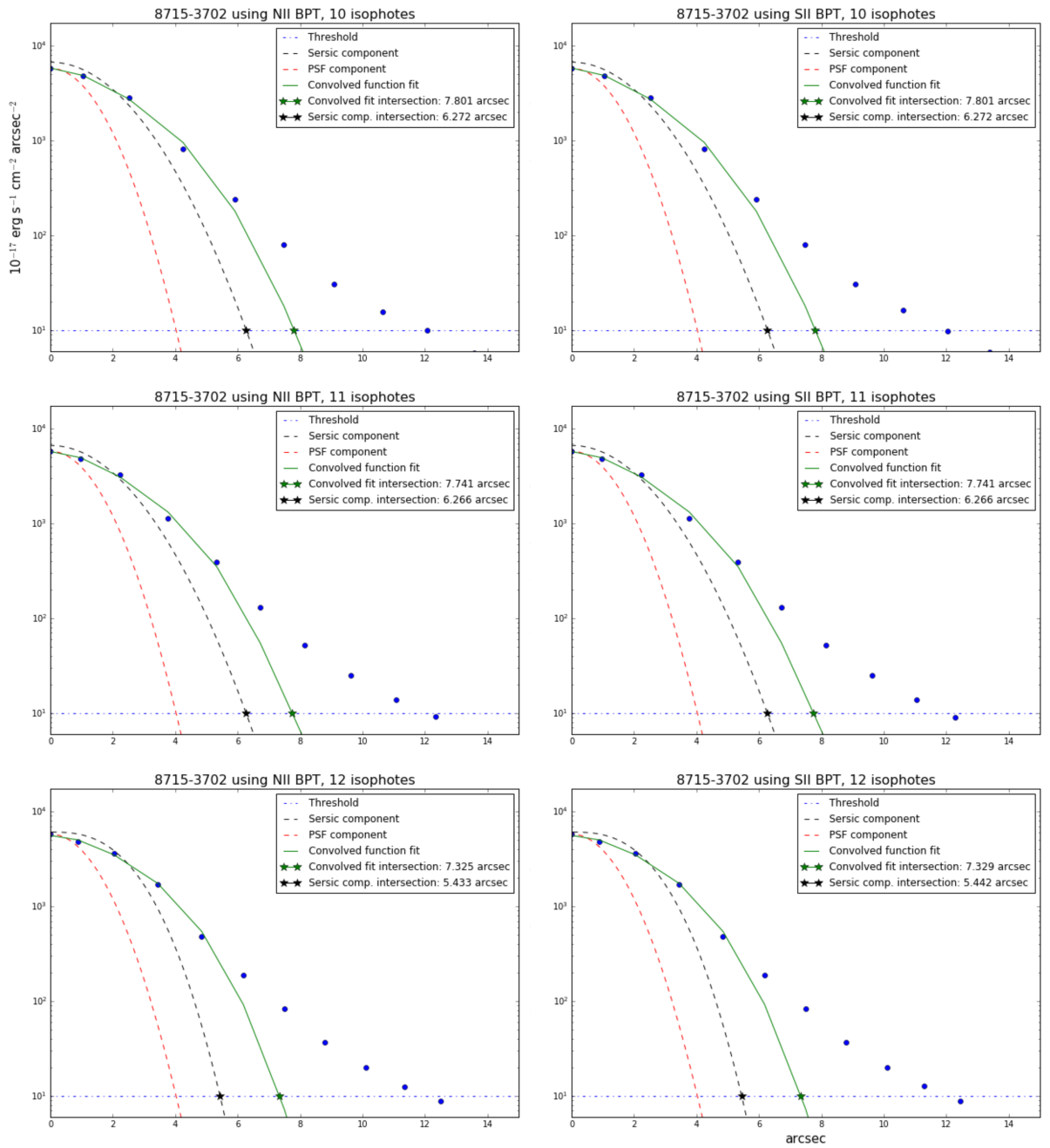
Fig. 7.9. Radial profiles of target 1-604907 derived from two different BPT diagnostics and three different numbers of isophotes.